Multi-scale strainfield analysis using geostatistics : investigating the rheological behavior of the hot Variscan crust of the Pyrenees (Axial Zone)

Bryan Cochelin, Charles Gumiaux, Dominique Chardon, Yoann Denèle, Benjamin Le Bayon

Accepted Manuscript

Multi-scale strainfield analysis using geostatistics: Investigating the rheological behavior of the hot Variscan crust of the Pyrenees (Axial Zone)

Bryan Cochelin, Charles Gumiaux, Dominique Chardon, Yoann Denèle, Benjamin Le Bayon

PII: S0191-8141(18)30174-3

DOI: 10.1016/j.jsg.2018.07.024

Reference: SG 3719

To appear in: *Journal of Structural Geology*

Received Date: 24 March 2018

Revised Date: 19 July 2018

Accepted Date: 30 July 2018

Please cite this article as: Cochelin, B., Gumiaux, C., Chardon, D., Denèle, Y., Le Bayon, B., Multi-scale strainfield analysis using geostatistics: Investigating the rheological behavior of the hot Variscan crust of the Pyrenees (Axial Zone), *Journal of Structural Geology* (2018), doi: 10.1016/j.jsg.2018.07.024.

Multi-scale strainfield analysis using geostatistics: Investigating the rheological behavior of the hot Variscan crust of the Pyrenees (Axial Zone)

Bryan Cochelin[1,2,3,*], Charles Gumiaux[3], Dominique Chardon[2,4,5], Yoann Denèle[2], Benjamin Le Bayon[1]

[1] BRGM DGR/GSO, BP 36009, 45060 Orléans, France

[2] Géosciences Environnement Toulouse, Université de Toulouse, CNRS, IRD, UPS, CNES, 31400 Toulouse, France

[3] Univ. Orléans, CNRS, BRGM, ISTO, UMR 7327, F-45071, Orléans, France

[4] IRD, 01 BP 182, Ouagadougou 01, Burkina Faso

[5] Département des Sciences de la Terre, Université Ouaga I Professeur Joseph Ki-Zerbo, BP 7021, Ouagadougou, Burkina Faso

Submitted to *Journal of Structural Geology*, 'from hot to cold' special issue, 24 March 2018

Revised: 19 July 2018

MARKED MANUSCRIPT

Modifications in blue – Additions in red

* corresponding author: bryan.cochelin.get@gmail.com

Abstract

The present study provides a quantitative way to analyze and interpolate strainfields from ductile fabric field measurements using geostatistics. Based on variogram analysis and kriging interpolations, the developed methodology allows computing automatic cleavage and lineation trajectory maps at different scales from a same field structural dataset. For the example provided by the hot Variscan crust of the Pyrenees, the analysis of cleavage/stretching lineations orientation and kinematic data document pure shear conditions recorded during convergence. Strain was vertically partitioned between an upper crust submitted to homogeneous thickening responding to N-S (orogen-normal) shortening and a hot and partially molten mid-lower crust affected by horizontal longitudinal (orogen-parallel) flow. The emplacement of plutons and gneiss domes generated heterogeneities in the upper crust and induced strain localization into steep anastomosed transpressional shear zones flanking those structures. The results show that geostatistics applied to structural geology are powerful tools for retrieving tectonic regimes of large orogenic segments by identifying and quantifying perturbations in the strainfields induced by protracted and potentially complex tectonic histories. The variogram analysis also gives first order clues to evaluate whether the considered structural domains underwent single continuous ductile or polyphased brittle-ductile deformation.

Keywords

Strain partitioning, variogram analysis, kriging interpolation, transpression, hot orogen

1. Introduction

Determination of principal strain and stress directions in the lithosphere has always been a key task for understanding and constraining plate tectonics. Mapping and analysis of strain/stress field patterns bring constraints on the mechanical behavior of crust/lithosphere. Such an approach allows evaluating (i) the meaning of spatial shear gradients and finite strain values in terms of displacement(s), (ii) the way deformation localizes, (iii) the role of rheological contrasts between adjacent lithologies during deformation and (iv) the rheological contrasts between structural levels and their degree of coupling. In active tectonic domains, approximate stress fields can be obtained using measured GPS velocity fields (e.g. Welsch, 1983; Kahle et al., 1999; Grenerczy et al., 2000, Zang et al., 2004; Titus et al., 2011) or focal mechanisms from earthquakes (e.g. McKenzie, 1972; Calais et al., 2002; Engdahl and Villasenor, 2002). Structural analyses of fractures and faults further allow retrieving paleo-stress fields (e.g. Angelier, 1984; Blès et al., 1989). For ductile deformation, foliation and stretching lineations can be considered as good proxies of principal strain axes orientations (Ramsay, 1967; Siddans, 1972; Wood, 1974). Foliation and lineation trajectories allow (i) investigating how the direction of principal strain axes change through space and (ii) deciphering homogeneous from heterogeneous strains by considering gradients and trajectory curvatures (i.e., convergence of trajectories) (see Cobbold and Barbotin, 1988). Following Cobbold and Barbotin (1988), the amount of strain is mostly difficult to quantify for natural case, therefore foliation and lineations trajectories – once coupled to a kinematic analysis of fabrics – are used to build paleo strainfields (or strain patterns). These trajectory maps are mostly extrapolated manually on the basis of structural measurements data (e.g. Brun and Pons, 1981; Brun, 1983; Chown et al., 1992; Gautier and Brun 1994; Bouchez and Gleizes, 1995). Moreover, extracting regional trends from individual local structural

measurements may not be straightforward and would hardly be reproducible in case of low data density at a considered scale. The resulting trajectory maps may thus be intrinsically qualitative.

Considering the limitations of manual strainfields' interpolation, geostatistics can be used to quantitatively analyze spatial variations in the orientation of structural measurements and to obtain the best fitted interpolated maps, whatever the scale considered. The general approach has first been introduced by Matheron (1962). Such geostatistical analysis has already been used for brittle deformation to retrieve stress fields using fracture or fault data set (Escuder Viruete et al., 2003; Rafiee and Vinches, 2008; Koike et al., 2015; Hanke et al., 2017; Riller et al., 2017) and 3D modeling of geological objects at local scale (e.g. folds, see Hillier et al., 2013; Grose et al., 2017). It has been also developed and successfully applied to the analysis of ductile fabrics directional data (Gumiaux et al., 2003). Based on a preliminary statistical analysis (the variogram analysis or variography), spatial interpolations can be computed, leading to automatic cleavage or foliation trajectory maps (Gumiaux et al., 2003, 2004).

In this study, we apply such geostatistical approach in order to obtain quantitative insights on the way strain has been spatially (i.e. horizontally and vertically) partitioned during convergence. Indeed, in orogenic contexts, geotherms control – at first order – vertical rheological layering and mechanical coupling in the lithosphere (Davy, 1986). Contrary to cold collisional belts such as the Alps and Taiwan (Brun, 2002; Lacombe and Mouthereau, 2002), old accretionary or mature orogens have undergone critical weakening on a lithospheric scale, inducing specific vertical strain partitioning pattern and mass redistribution between the upper crust and a particularly weak lower crust (Chardon et al., 2009). In order to investigate such space-time strain partitioning patterns, the present study focuses on a segment of the Variscides exposed in the Pyrenees, which underwent both thickening upper crust and the laterally flow of its mid-lower crust (Cochelin et

al., 2017). In a first step, processing of the overall structural dataset allows producing a strain trajectory map corresponding to the total finite strainfield of this crustal segment. Strainfield is then successively deconvoluted to constrain strain interference effects induced by crustal domains or units of contrasted mechanical behaviors (i.e. the upper crustal metasediments, the mid-lower crust and plutons). The analysis of strainfields based on strain trajectory modeling is performed from regional to local scale, with some focuses made on the Canigou gneiss dome and the Mt-Louis pluton.

2. Geological setting

The Pyrenees form an east-west trending intra-continental mountain range resulting from the collision between the Iberian and the European plates (Choukroune, 1992). During upper Cretaceous to Early Tertiary convergence, shortening was responsible for the exhumation and erosion of the Mesozoic cover, allowing exposure of the Paleozoic basement, which preserves Variscan (i.e., Late Paleozoic) orogenic deformation patterns. This portion of the Variscan orogen corresponds to the foreland of the belt and occupied the core of the Iberian-Armorican syntax during the latest stages of the orogeny (310-290 Ma) (Cochelin et al., 2017). The largest uplifted unit of pre-Mesozoic rocks outcropping in the Pyrenees is called Axial Zone and forms the core and highest part of the Cenozoic belt (Fig. 1a). Differential denudation of the Axial Zone provides an access to a continuous vertical section of the Variscan crust from the shallowest parts in the west (i.e. Carboniferous sedimentary basins) to mid-crustal levels in the east. Despite the "recent" (i.e., Alpine) Pyrenean orogeny, the structural continuity of the Variscan crust is maintained in the Axial Zone; which forms a consistent tectonic domain affected by only local and moderate perturbations due to post-Paleozoic deformation (Zwart, 1986; Carreras and Debat,

1996, Carreras and Druguet, 2014, Cochelin et al., 2017, 2018). The present study focuses on the pre-Mesozoic Axial Zone.

Figure 1 here

The Axial Zone is mainly made of Ediacaran to Upper Carboniferous sedimentary rocks having undergone High Temperature-Low Pressure (HT/LP) metamorphism that induced regional partial melting (Guitard et al., 1996 and references therein). These metasedimentary rocks were intruded from ca. 310 to 290 Ma by large calc-alkaline plutons (Denèle et al., 2014 and reference therein). Two contrasted structural levels are distinguished (de Sitter and Zwart, 1962; Zwart, 1979; Carreras and Capella, 1994). The low-grade metasedimentary rocks belonging to the upper crust are characterized by open to tight EW trending folds and steep N95-110°E striking axial plane cleavage (Figs. 1b & c) bearing steeply plunging stretching lineations (Cochelin et al., 2017, 2018). The average strike of cleavage around N100°E associated to an average pitch of lineations around 83°W is compatible with transpression due to ~NS shortening (Cochelin et al., 2017). The lower structural level comprises the partially molten mid-lower crust that appears in gneiss domes elongate parallel to the regional structural trend (Figs. 1a & c) and mostly bearing longitudinal stretching lineations (Carreras and Debat, 1996; Mezger and Passchier, 2003; Denèle et al., 2007; 2009; Cochelin et al., 2017). The chronological and structural relationship between steep and shallowly dipping structures has been subjected to debates since the 60's (e.g. de Sitter and Zwart, 1960; Zwart, 1979; Soula et al., 1986; Carreras and Capella, 1994; Carreras and Debat, 1996) but recent structural studies, especially within calc-alkaline plutons and gneiss domes, showed that they were formed during a single, protracted period of deformation, under dextral transpressional regime (Bouchez and Gleizes, 1995; Gleizes et al., 1998; Mezger and Passchier, 2003; Aurejac et al., 2004; Vilà et al., 2007; Denèle et al., 2007; 2008; 2009; Mezger, 2009;

Cochelin et al., 2017 among others). In spite of the N-S convergent context, HT-rock of the mid-lower crust were exhumed in gneiss domes (Mezger and Passchier, 2003; Vilà et al., 2007; Aguilar et al., 2015). This has been favored by strain localization near the biotite-andalusite transition, forming retrogressive extensional shear zones (Van den Eeckout, 1986; Van den Eeckout and Zwart, 1988; Mezger and Paschier, 2003; Cochelin et al., 2017) while the core of the domes was affected by horizontal longitudinal flow (Denèle et al., 2007; 2009; Mezger, 2009; Cochelin et al., 2017).

Figure 2 here

The transition between the thickening upper crust and the laterally flowing lower crust is well exposed in the Central and Eastern Pyrenees by the succession of ~EW trending regional scale synforms and gneiss domes (e.g. the Villefranche syncline and the Canigou gneiss dome, see Figs. 1c & 2). The Canigou gneiss dome is characterized by a pervasive foliation reworking Ordovician plutons turned into orthogneisses and their country-rocks (Fig. 2, Casas et al., 2010; Martinez et al., 2011). Stretching lineations are mainly NE trending in the core of the dome and are associated with dominant top-to-the SW shearing (Guitard, 1960; Soliva et al., 1989; Carreras and Debat, 1996; Cochelin et al., 2017). This massif was lately cut by post-Paleozoic faults like the Alpine Canigou Thrust and the Neogene Têt-Cerdagne and Py-Fillols faults (Fig. 2). Immediately to the north west of the Canigou gneiss dome crops the Mt-Louis pluton, which was emplaced at ca. 301-303 Ma (Figs. 1a & 2) (Denèle et al., 2014). It shows a complex internal structure and can be divided into three subintrusions (Bouchez and Gleizes, 1995) and, like most plutons in the Axial Zone, this pluton was deformed under sub-magmatic to solid-state conditions (Bouchez and Gleizes, 1995; Debon et al., 1996, Denèle et al., 2014). The Canigou and Mt-Louis massifs can be regarded as demonstrative examples of gneiss dome and pluton of the Axial Zone,

156 respectively. Focus analyses of local scale strainfields are made on these massifs in the present
157 study.

158 **3. Methodology and data set**

159 The computation of cleavage trajectory maps results from an interpolation process of the striking
160 value between individual structural measurements. This technique allows imaging the continuous
161 spatial variations of the finite strain field that can be deduced from discrete natural observations.
162 Thereby, some difficulties may arise when measurements (i) are heterogeneously distributed
163 through the area and/or (ii) display significant local-scale variations in orientation. In particular, it
164 is often not straightforward when one has to *a priori* choose whether to highlight local tendencies
165 or regional ones through a hand drawing process, using curvy or smooth trajectories shape,
166 respectively. Here, we employ a geostatistical approach to automatically map both cleavage and
167 lineation trajectories and cleavage dip angle variations from a given field structural dataset.
168 Ideally, interpolations should be made from foliation-lineation pairs in order to integrate the full
169 information of the finite strain ellipsoid's orientation (see the critical review of Davis and Titus,
170 2017). However, such approach requires a very homogeneous dataset in which each lineation
171 trend/plunge measurement can be associated to a foliation strike/dip one and vice versa. In the
172 case of regional-scale studies (as the one exposed here), structural data are often compiled from
173 various types and ages (e.g. digitized maps from PhD theses, articles), and such a prerequisite is
174 unfortunately hardly tenable. Alternatively, structural data sets can be decomposed into four one-
175 dimensional numbers (i.e. strike, dip, trend and plunge) and analyzed separately. While dip value
176 is interpolated using simple kriging on a scalar variable (for a 0-90° range in that case), kriging
177 interpolation of the strike value (which is of circular data type) is performed following the
178 approach developed by Gumiaux et al. (2003). Based on a theoretical and unscaled case study

179 (see Figs 3 & 4), details of the different steps of our approach developed are given below (3.1)
180 and, in particular, some keys for the pre-interpolation variogram analysis (3.2). This synthetic
181 cleavage and stretching lineation dataset simulates interactions between a roughly E-W regional
182 trending structure and termination of an elliptical body, to the west, which may correspond to an
183 intrusion. It results in a triple point as visible in the center of the map (Fig. 3.1).

184 *3.1. Computation of automatic trajectory maps*

185 The computation process has been developed in a GIS environment and all the structural
186 measurements are firstly compiled into a spatial database (37 cleavage orientation measurements
187 in the synthetic case study, with 20 stretching lineations; Fig. 3.1). Secondly, spatial variations of
188 the dataset values can be quantified by the computation of experimental variograms (Figs 3.2 &
189 4.2) (Matheron, 1962). Initially developed for mining purposes and applied to scalar values
190 (Matheron, 1962), this method has been adapted by Gumiaux et al. (2003) for the analysis of
191 circular angular variables such as structural striking data. The goal is to assess the degree of
192 correlation between values of the studied variable (e.g. azimuth or dip of cleavage data) measured
193 at different locations and according to the interdistance separating them. If this correlation degree
194 changes with increasing interdistance, the variable is thus categorized as regionalized. The
195 variogram analysis allows (i) quantifying the maximum distance to which distant data values
196 show significant mutual dependence, (ii) constraining their dependence function to the distance,
197 (iii) deciphering any potential anisotropy in the spatial variations of the regionalized variable and
198 (iv) given the scale of the study area, filtering “regional” and “local” variation trends from the
199 dataset (see details in the next section). In a third stage, kriging interpolation can be achieved on
200 both the dip values and azimuth directions following the method developed by Gumiaux et al.
201 (2003) for circular data. Kriging weights are computed based on a given theoretical variogram

model whose equation has been adjusted – for each data set – to the parameters deduced from the detailed variogram analysis (parameters include the function type, the *range* value, the proportional *nugget effect* and *sill* values; see part 3.2 below). In the example, interpolations allow obtaining cleavage direction map, cleavage dip map (Fig. 3.3) or lineation trend maps (Fig. 4.3), as continuous grids covering the overall study area, and where corresponding data is available. During the two-fold computation/interpolation of the directional map, the local direction variance can be estimated using the parameter R, which reflects the degree of dispersion of data (Upton and Fingleton, 1989). In [0,1], low R values reflect high variation in measured direction values for short distances, whereas a R of a theoretical maximum value of 1 reflects strictly parallel cleavage directions in the neighborhood (see Gumiaux et al., 2003 and Figs 3.3c & 4.3b). In the example, low R values computed from the cleavage data point to significant directional variations induced by the eastern termination of the elliptical body and its associated cleavage triple point (forming a singular point; see Fig. 3.3c). In contrast, the trend of stretching lineations shows only minor variations for short distances with R values above 0.5 for most of the study area (Fig. 4.3b). Trajectories are then computed, giving a good picture of variation of cleavage directions at the scale of the studied area and reproducing at high resolution cleavage singular points (including neutral or triple points), both within and outside the simulated intrusion, and small scale variations within the elliptical geological body (Fig. 3.4). Besides, the continuous and radial distribution of stretching lineations, as implied by dataset in Figure 3.1, is also well-modeled and imaged following this fully automatic process (Fig. 4.4). In order to better constrain the strain field geometry, trajectory maps can be superposed over the interpolated dip angle map. In the example case study, shallow dipping cleavage areas correspond to the elliptical shape structure to the west and to more scattered cleavage direction zones, as highlighted by rather high R values (compare maps in Figs. 3.4 & 4.4). Note that the low R values obtained in

low dip domains may be oversighted compared to those from steep cleavage domains as this analysis of cleavage direction was performed in 2D (i.e. map view). Indeed, strike value of sub-horizontal fabrics (i.e. < 20°) may significantly vary in response to local orientation perturbations.

Figure 3 here

Figure 4 here

3.2. Variogram analysis

As a general principle, two close data measurements may have more similar values than two distant ones. Yet, superimposed phenomenon at different scales can control variations in the regionalized variable. For instance, cleavage orientation can result from the combination of (i) a tectonic regional-scale maximum shortening direction, (ii) influence of the expansion of a neighboring synkinematic intrusion (medium-scale) and (iii) very local cleavage refraction due to lithological contrast in the rock unit considered. Thus, in order to determine and evaluate the mutual dependence between data values, experimental variograms are calculated as a squared root difference between individual angle values as a function of their separating distance (Figs. 3.2 & 4.2); increasing values with distance show decreasing correlation between data values with a rate depending on the steepness. Thus, the shape of the resulting experimental variogram plot gives key information on the spatial structure of the strain field. This is estimated by fitting a theoretical function to the experimental variogram (see continuous grey curves in Figs. 3.2 and 4.2) and extracting several parameter values from the latter, as detailed below (see Matheron, 1962 for details). Acceptable functions include spherical, exponential or Gaussian.

- An increasing variogram can reach a constant *sill* value for a maximum correlation *range* distance value (Fig. 3.2 left) and is then defined as *stationary*. This shows that the kinematical and/or rheological phenomena controlling the spatial strain variations have a distance of influence shorter than the maximum width of the study area. In the synthetic example, the *stationary* cleavage directions variogram highlights deformation process with effects over 9 to 10 distance units (Fig. 3.2 left). This feature is also consistent with the computed trajectory map which displays the overall structure of the junction area (Fig. 3.4). On the contrary, the *non-stationary* variograms computed for the lineation directions or cleavage dip angle show that the phenomenon driving strain orientation's variations has some influence out of scale of the study area (i.e. *range* is not reached, Figs. 3.2 right & 4.2),
- Adjustment and analysis of the trend of the variogram for shorter distances is of primary importance and in particular its initial slope characterizing the type of influence linked to the phenomenon. Exponential function (Fig. 3.2 left), for instance, displays a notably quick increase from its original. This corresponds to continuous spatial variations in the strain direction but with a rather limited size (or rapid decrease) of influence. In the synthetic example, such feature is attested to by the narrowness of triple junction's zones and rather high curvature of the trajectories there (Fig. 3.4). In contrast, the Gaussian theoretical variogram function displays a nearly null slope from its origin (Fig. 4.2) showing a very slow decrease of influence of the phenomenon in space. This is expressed in the strain field by low curvature and very smooth variations in the trajectories pattern (Fig. 4.4).
- Finally, a non-null ordinate value at the origin of the variogram – the *nugget-effect* – reflects some variations in the strain field that cannot be considered regarding the given

density of the data points. This includes a proportion of either background noise in the dataset (i.e. different kinds of uncertainties or errors made during the acquisition process), very local rheological effects (such as cleavage refraction in layered rocks for instance) that can be regarded as insignificant at the scale of the strain field considered, or both. In the synthetic case study presented here, the variogram computed for stretching lineations direction measurements displays a null *nugget effect* (original variogram Γ is zero, Fig. 4.2). This corresponds to an idealistic situation where neither measurement error nor very local deviation effects exist in the dataset and 100% of the cleavage direction variations can be modeled in the trajectories map computation. For natural case studies, a significant proportion of the variance may be included in the *nugget* and, thus, not modeled.

In order to detect potential anisotropy in strainfield variations, *directional* individual variograms can be calculated by selecting data pairs along predefined space direction classes. This technique is particularly efficient (i) to quantify the *range* of significant variations of values in the investigated directions and (ii) to highlight main structural anisotropies such as folds or sigmoidal trends induced by regional shearing (Gumiaux et al., 2003, 2004, Branquet et al., 2012).

3.3. Data set

All the structural data available to date in the Axial Zone of the Pyrenees (Cochelin et al., 2017) have been treated. This extensive structural compilation (see supplementary materials) comprises 14 275 cleavage and foliation plane measurements, including 12 665 with dip information and only 1 623 mineral-stretching lineations. At first, analysis and interpolation of structures' orientation is performed for the entire dataset over the Axial Zone. Then, in order to deconvolute the finite strain field, three distinct structural sub-sets have been selected based on the type of geological units in which structural measurements have been made: (i) a first set for the upper

crustal metasedimentary rocks called hereafter ‘upper crust’ comprising 5 366 cleavage planes and 272 stretching lineation measurements, (ii) a second set for the plutons comprising 3610 foliation planes (with a zoom on the Mt Louis pluton) and (iii) a third set for mid-lower crustal rocks called hereafter ‘mid-lower crust’ including 5 299 foliation planes and 1 351 mineral-stretching lineation measurements (with a zoom on the Canigou gneiss dome). Spatial selection have been made using digitalized outlines of the corresponding units in the maps. Cleavage/foliation data points are spatially duly distributed over the Axial Zone (see supplementary materials) and the strikes show a normal distribution centered on N96.5°E and a skewness factor of about 0 (nonparametric skew used here; Fig. 5a). Cleavage strikes from the mid-lower crust follow a very similar normal distribution (Fig. 5b) with a mean value at N94.6°E. In contrast, the directional data from the upper crust are skewed to the left and show a mean value of N102°E (Fig. 5c). For the whole Axial Zone, the dip values of cleavage/foliation data show a mean value of 51° and a skewness around 0 (Fig. 5d). In the middle crust, dip values also show a skewness about 0 with a mean value of 47° (Fig. 5e) while data in the upper crust are skewed to the steep values and show a mean value of 51° (Fig. 5f). In the whole data set, flat-lying foliations (i.e. < 20°) represent less than 7% of the measurements. Therefore, their relative impact on interpolations of strike values can be considered as negligible in the present case study. Stretching lineations have principally been measured in gneiss domes. Considering their data points’ spatial distribution, geostatistics were applied to mid-lower crust and solely statistics for upper crust data.

Figure 5 here

4. Results

4.1. Axial Zone strain field

317 The omni-directional variogram for the Axial Zone dataset displays a sill reached for a 10km
318 general range value (grey dots/black curve, Fig. 6a). An abrupt change in slope at 1.8km indicates
319 a second, intermediate range, which indicates the change to a different structuration, from local to
320 more regional scale phenomenon effects. As a whole, this variogram can be modeled with (i) a
321 nested (or imbricated) structure of two spherical functions of distinct range values and (ii) a
322 global sill of 1095 square degrees and a nugget-effect value of 503 square degrees (corresponding
323 to 46% of the total variance for this dataset).

324 The omni-directional variogram obtained for dip measurements over the Axial Zone shows an
325 exponential trend, reaching a sill of about 480 square degrees at a 21 km range and showing 60%
326 of proportional nugget effect (grey dots/black curve, Fig. 6b). The later suggests, on average, a
327 significant variability of the dip values measured over short distances (i.e. distances shorter than
328 1 km).

329 Figure 6 here

330 Based on the variograms (Fig. 6a), interpolation of cleavage trajectories at the scale of the whole
331 Axial Zone was performed using a 10km range. In this case, the interpolated trajectories display
332 an average N100°E parallel trend over most of the Axial Zone and rotates to an average of
333 N130°E in eastern part of the Axial Zone (Fig. 7a). Based on the R parameter map (Fig. 7b),
334 domains belonging to the upper crust show limited cleavage strike dispersions (with R values
335 above 0.5). This is also shown by the regular trend of the trajectory map in the upper-crust
336 domains and especially in a ~30km wide N-S corridor displaying sub-parallel trajectories in
337 Central Pyrenees (Fig. 7b). This corridor is devoid of plutons (see Figs. 1b & 7a), suggesting a
338 role of such intrusions in local- to intermediate-scale variations of the upper crust strainfield.

Figure 7 here

Interpolation of cleavage dip values for the whole Axial Zone dataset (Fig. 8a) displays a clear N-S segmentation, with steep cleavage in a northern domain and shallowly dipping cleavage in a southern domain. This N-S fanning of cleavage dip is well expressed, especially in the ~N-S corridor of sub-parallel trajectories referred to above (Fig. 7b). This variation corresponds to the fan of cleavage that had been early noticed by Zwart (1979) in this region. Calculation of the gradients between interpolated dip values (Carrara et al., 1991) allows identifying zones or bands with rough variations of dip, and, in another hand, undisturbed domains such as in the upper crust level (Fig. 8b; note in particular the delineation of the ~NS corridor in the central part).

At second order, the strain field appears rather heterogeneous. Gneiss domes and plutons are very well individualized and evidenced by circular to concentric trajectories (Fig. 7a). Heterogeneity is also highlighted by converging and tightening of the trajectories underlining at least 5 longitudinal 100 to 150 km long shear zones. They mostly trend ~N100°E and locally N130°E, where they wrap around gneiss domes and plutons. Trajectories that converge in N100°E trending bands show rather symmetrical pattern with both clockwise and counterclockwise rotations on both sides of these bands. In contrast, N130°E trending bands induce convergence and bending of trajectories as smooth sigmoids. Such sigmoidal patterns (i.e. asymmetrical) for trajectories are compatible with dextral shearing (Fig. 7a) (Ramsay and Graham, 1970). These sigmoidal patterns form locally asymmetrical singular points (neutral or triple points) at western and eastern tips of elliptical bodies (e.g. around the Néouvielle pluton), which is also compatible with dextral shearing. Otherwise, cleavage singular points at eastern and western terminations of the domes and plutons appear mainly symmetrical in respect of the elongation axe of these domes and plutons.

Figure 8 here

Thus, the upper-crustal cleavage appears disturbed only around granitic plutons with particularly low R values coinciding with (i) cleavage singular points and (ii) some known composite plutons showing internal imbricated magmatic structures (e.g. Cauterets plutons, Fig. 7b). In the eastern part of the Axial Zone, high dispersion zones (i.e. with low R values) surround the gneiss domes. Some folded gneiss domes display internal dispersion too (e.g. the Aston gneiss dome, see Denèle et al. 2009). Discrete dispersion bands, sometimes oblique to the cleavage trajectories, are also mapped within gneiss domes, like in the Canigou (Fig. 7b). This kind of dispersion could be related to post-Variscan faulting (see section 4.4).

The impact of gneiss domes and plutons on the regional strainfield is also well shown by cleavage dip variations (Fig. 8b) outlining concentric shapes and reflecting short-length gradients between the cores and envelops of these bodies (e.g. the Cauterets plutons). Other short-wavelength variations that are not directly related to domes or plutons display highly to slightly oblique trends to trajectories. For instance, N60° to N80°E trending bands are detected south of the Canigou gneiss dome. This reflects late tilting of the cleavage along Neogene normal faults as well as Alpine thrusts (Fig. 8b). The relative scarcity of such perturbations shows that the Variscan structures are only weakly affected by post-Paleozoic deformation phases within the Axial Zone (see Cochelin et al. 2017, 2018).

As a whole, the overall strain field looks homogenous on a regional-scale and locally disturbed by the presence of gneiss domes and plutons, forming areas with curved cleavage trajectories and lower dip values (e.g. in eastern Axial Zone).

4.2. Upper crust

384 The omni-directional variogram computed for the upper crust dataset (blue dots/curve, Fig. 6a)
385 shows an exponential trend with a significantly lower variance (849 square degrees) than that of
386 the entire data set, but a similar nugget effect proportion (47%). The best-fitted theoretical
387 variogram suggests an intermediate range at ca. 5 km. The four directional-variograms display a
388 same trend than the omni-directional one (compare Figs. 6a & 9a, b) with similar range (5km),
389 sill (810 square degrees) and proportional nugget effect (between 47 and 53%) values. The NE-
390 SW (i.e. from N22.5° to N67.5°E) trending directional-variogram differs from the others, with a
391 sinusoidal trend of periodicity around 18 km. This illustrates systematic regional scale
392 undulations of directional data, along the NE-SW direction (i.e. forming perpendicular ~NW-SE
393 striking bands like).

394 Figure 9 here

395 Considering cleavage dip values in the upper crust, the omni-directional variogram is similar to
396 that of the entire Axial Zone dataset but tends to show a greater instability (blue dots/curve, Fig.
397 6b). Directional-variograms are calculated from dip measurements parallel and perpendicular to
398 the average cleavage strike (i.e. ~N100°E, Fig. 9c). The “parallel” N100°E directional-variogram
399 has an exponential trend with a 5km range (much shorter than for the omni-directional
400 variogram) and a proportional nugget effect around 52%. In contrast, the “perpendicular” N10°E
401 oriented directional variogram (Fig. 9d) displays an exponential trend but is non-stationary (it
402 does not reach a sill up to the maximum possible 40 km computational distance). The latter
403 depends on the N-S width of the Axial Zone and on the critical number of data pairs available for
404 calculation, which dramatically decreases beyond 40km and makes the variogram unstable (Fig.
405 9d). These two directional-variogram show that cleavage dip value does not have regional-scale
406 variations along strike in the upper crust, whereas such variations are evidenced in the N-S

direction, perpendicularly to the fabric. Following the exponential best fit function on the 40 first kilometers, the range of the N-S directed variogram and the characteristic distance of influence of the corresponding phenomenon could be reached around 80-100km. This variation can be related to the regional N-S fan of schistosity (section 4.1).

Interpolations of cleavage directions have been performed up to 20 km interdistance, which corresponds to the largest range revealed by the variogram analysis of the upper-crust (i.e. in directional variogram, Fig. 9a). Regional trajectories computed from the sole upper crust are roughly parallel. They display an overall arc shape (Fig. 10a) from N110°E trends in the western part of the Axial Zone, longitudinal trends in the central Axial Zone to N130-140°E trends in the easternmost Axial Zone, which is quite similar to trajectories obtained in Fig. 7a. At second order, E-W elongated lens patterns can be deciphered in the Eastern Axial Zone. In the western Axial Zone, trajectories are weakly disturbed and only display a few variations over short (<10 km) wavelength undulations. The convergence of N110°E trending trajectories in the median part of the Axial Zone (e.g. between Ct and Nv) and disappearing to the east is the only apparent regional strain gradient revealed by the interpolation (Fig. 10a). Indeed, the rather consistent spacing of the trajectories indicates a more homogeneous strain pattern than obtained using the entire data set (Fig. 7a). Similarly as on the first trajectory map, singular points are symmetrically displayed at western and eastern tips of the 10 to 20 km elliptical bodies and aligned along the cleavage mean trend (Fig. 10a). The only asymmetrical converging pattern (i.e. sigmoidal) of trajectories are located, from west to east, around the Chiroulet-Lesponne domes (CL), the Néouvielle plutons (Nv) and the eastern part of the Canigou dome (Ca) (Fig. 10a). These sigmoidal trajectories again suggest dextral shearing within shear bands.

Figure 10 here

The interpolation of cleavage dip values for the upper crust data set upholds a NS segmentation over the Axial Zone (Fig. 10b) with a northern part showing steep to vertical cleavage and a southern one where the cleavage is progressively tilted southward to reach moderate to low northward dips. In the Eastern Axial Zone, this segmentation of cleavage dip is still visible but is disturbed by the influence of gneiss domes and plutons (compare Figs. 1a & 10b). In central and western Axial Zone, the influence of Bossost and Chiroulet-Lesponne domes is also documented by two "anomalies" of shallowly-dipping cleavage inside the northern steeply-dipping domain (Fig. 10b). Even though only the upper crust structural dataset is considered in the present interpolations, both cleavage trajectories (showing lens shapes map structures) and interpolated dip map display anomalies surrounding gneiss domes and plutons (compare Figs. 7 & 10).

Whatever the cleavage dip, stretching lineations measured in the upper crust are, in most cases, characterized by high pitch values (>60° for 61 % of the set). As cleavage is mostly steeply dipping (Fig. 1b & 10b), lineations often have high plunges. In regional shear zones (Figs. 1 & 7a), lineations are associated with either dip-slip or reverse sense of shear with minor dextral component (Cochelin et al., 2017, 2018). If plotted in a Dip-Pitch-Plunge ternary diagram (Fig. 11-left; see Chardon et al., 2009), two distinct sub-populations are identified. Most of the dataset shows a trend from the vertical flow to the horizontal flow pole, which reflects a decrease of foliation dip with nearly constant high pitch values. The remaining part of the data is closer to the Orogen-parallel "strike-slip" flow pole, reflecting lower pitches on steep planar fabrics (Fig. 11-left). At very first order, the upper-crust is thus characterized by (orogen-normal) horizontal shortening and (sub-) vertical stretching. In more details, variations from the vertical to the horizontal flow poles can be related to (i) the regional-scale N-S segmentation of the upper-crust strain in two main cleavage dip domains (Fig. 10b) or (ii) the shallowing of upper crust cleavage

around the domes (e.g. the Bossost dome and the Canigou dome, Fig. 10b). Furthermore, at a third order, the dispersion of the data between the vertical flow pole and the orogen parallel "strike-slip" flow pole (left axis of the triangle plot) reflects strain partitioning within strike-slip dominated transcurrent shear zones. In the Axial Zone, these shear zones – mainly N120-130°E trending – show dextral-reverse kinematics and are flanking gneiss domes and plutons (Cochelin et al., 2017; e.g. the Mérens and Têt shear zones; Fig. 7a).

Figure 11 here

4.3. Upper crustal plutons: focus on the Mt Louis massif

The omni-directional variogram computed from the fabric direction measurements in the Mt Louis pluton (extracted from Anisotropy of Magnetic Susceptibility - AMS - foliation orientation extracted for each station of Bouchez and Gleizes, 1995) is stationary (Fig. 12a): it reaches a 1142 square degrees sill at 3.4 km range and includes 54% of proportional nugget effect. The global cleavage direction variance for this pluton (corresponding to the sill) and its variability at very short distances (the nugget) are similar to those obtained for the global omni-directional variogram computed for the entire Axial Zone (Fig. 6a). This suggests that this massif – and certainly plutons in general – are of prime importance in the structuration of the strainfield. Yet, the Mt Louis experimental variogram displays a distinct range value and follows a Gaussian trend (with flat behavior close to the original) corresponding to particularly smooth tendency variations of the cleavage directions at the scale of the pluton. The regional interpolation (Figs. 7a & 12b) over the Mt Louis pluton and its wall rocks is characterized by longitudinal trajectories on the central-western part of the pluton with large and smooth undulations, whereas the concentric trajectories inside the pluton is only and roughly evidenced in its eastern part. As expected, the resulting interpolated trajectories at local-scale are more sensitive to local variations than those

obtained with larger range parameters (compare Fig. 12b & c). The sub-massifs are well individualized by concentric trajectories patterns, as exemplified in its western and eastern parts. These concentric patterns are in agreement with the trajectories obtained manually by Bouchez and Gleizes (1995) (Fig. 12d). Furthermore, our interpolations looks delineating three NW-SE bands showing asymmetrical converging trajectories (s-shape sigmoidal structures) coinciding with dextral shear zones inferred by Bouchez and Gleizes (1995) (Fig. 12d). Even though interpolated sigmoids are compatible with apparent dextral shearing (Fig. 12c), trajectories display very smooth variations and non-localized/pervasive shearing.

Figure 12 here

4.4. The lower crust and focus on the Canigou dome

The omni-directional variogram of the mid-lower crust exposed in the domes displays, as a whole, a slightly higher variance (i.e. average sill) and higher proportional nugget effect values (50%) than for the entire Axial Zone dataset (orange dots/red curve Fig. 6a). It shows a nested structure with (i) an exponential evolution up to 6-7 km and, beyond, (ii) a sinus trend of 15-20 km periodicity around the average sill (Fig. 6a). Such a rhythmic variogram can be related to the peculiar spatial distribution of measurements, which form evenly spaced clusters centered on the gneiss domes. The periodicity may thus simply reflect the average size of these domes, which is known as a hole-effect.

Focusing on the Canigou dome, the local-scale omni-directional variogram computed for cleavage striking data is stationary. It displays a lower maximum range (5 km) and a lower proportional nugget value (~38%) than the regional-scale one (compare Figs. 6a & 13a). This indicates less variable cleavage orientations and thus a more consistent strain field when focusing

498 on the lower-crust. The variogram follows an exponential trend corresponding to a rapid
499 decreasing effect of the phenomena with distance. The interpolated foliation trajectories reveal
500 two half domes (Fig. 13b), with E-W hinges. Considering the R parameter (Fig. 13c), the contact
501 zone between the two sub-domes coincides with a N50°E to N80°E trending band of highly
502 dispersed cleavage directions. The high-R band actually coincides with the Neogene Py-Fillols
503 normal faults, which cross-cuts the gneiss dome. Besides, the low-R domain at the south-eastern
504 boundary of the dome also appears to be related to post-Variscan faults and reflects the local
505 impact of the South Canigou Alpine thrust (Fig. 2) as suspected from the regional-scale map (Fig.
506 7b).

507 Figure 13 here

508 The stretching lineations measured within (Fig. 14a) the Canigou dome display only limited
509 variations in direction. The omni-directional variogram (Fig. 14b) is characterized by a high
510 ~57% proportional nugget effect and is defined by a sinusoidal trend. The interpolated
511 trajectories of stretching lineations exhibit an overall NE-SW trend (in red, Fig. 14c), with a very
512 smooth pattern. In contrast to the cleavage measurements, lineations do not show disturbance that
513 could be related to post-Variscan faulting. Indeed, the Py-Fillols faults are sub-parallel to the
514 lineation trajectories and the latter thus look poorly affected by late brittle deformation. First
515 order stretching trajectories are oblique on the hinge of the dome (compare Figs. 13b & 14c). In
516 greater details, trajectories display a systematic and progressive curvature, stretching becoming
517 progressively more transverse along the dome's limbs than in its core. This defines a map radial
518 trend from NE-SW in the lowermost structural levels of the dome to a NNE-SSW direction in the
519 southern limb and up to NW-SE trend in its north-western part. This latter trend is not well
520 expressed because the northern flank of the dome is actually truncated by the Neogene Têt-

Cerdagne fault (Fig. 2). As a whole, interpolated cleavage and lineation trajectories within the Canigou massif thus look particularly smooth and continuous; cleavage is only disturbed by significant but quite local effect of recent faulting.

Figure 14 here

Considering the overall Axial Zone, the average stretching direction is c.a. N98°E in the mid-lower crust (Fig. 15a) and, in a Dip-Pitch-Plunge diagram, data are clustered close to the orogen-parallel horizontal flow pole (Fig. 11-right). Dispersion of lineations towards the orogen-parallel "strike-slip" flow pole (Fig. 11-right) must be due to the late amplification of gneiss dome by folding, producing steep to overturned southern limbs in some cases (see Denèle et al., 2007, 2009, Vilà et al., 2007, Cochelin et al., 2017). In greater details, stretching lineations display two distinct direction families with regard to the gneiss domes' cartographic long axes. Longitudinal to slightly oblique stretching/flow is dominant, representing ca. 90% of the measurements within the domes (see the above described focus on the Canigou). Transverse stretching directions (i.e. NS trends) are restricted to the domes' envelope and represent only 10% of the exposed middle crust (Figs. 15a & 15b). In details, oblique WNW-ESE to NW-SE trends are documented in the core of all gneiss domes from the northern and western parts of the Axial Zone (i.e. Aston, Lys-Caillaouas, Bossost, Chiroulet and Lesponne domes) and from the Albères massif to the East (Fig. 15b). Purely longitudinal stretching is restricted to the Hospitalet dome while the Canigou shows a specific ENE-WSW trend (Figs 15b). Transverse stretching directions are observed in the envelope of the Chiroulet, Aston and Canigou domes and can be noticed in the Bossost dome (Fig. 15b). In the Chiroulet and Aston, the transition between longitudinal and transverse direction of stretching is abrupt, whereas it appears to be more gradual from the core to the limbs of the Canigou, Hospitalet and the Bossost domes (Fig. 15b). We consider the direction of

stretching in the core of gneiss domes as representative of the deep flow within the crust while direction of stretching in domes' envelope is related to their exhumation (Cochelin et al., 2017).

5. Discussion

5.1. Strain partitioning and crustal flow in the Variscan crust of the Pyrenees

The variogram calculated for the upper crust is stationary and shows the minimum of all the global variances (i.e. *sill* values) calculated in this study (compare variograms in Fig. 6). Such features reflect an overall steady strain direction throughout this domain, which bears the regional structural grain (Fig. 7a). Regional-scale interpolated cleavage trajectories for the upper crust are longitudinal and roughly collinear (Fig. 10a), which is typical of homogeneous deformation (Choukroune et al., 1995). Such cleavage trajectories pattern coupled with a dominant steep stretching (Fig. 11-left) is compatible with a bulk pure shear dominated deformation regime (Tikoff and Greene, 1997; Teyssier and Tikoff, 1999) with ~N-S horizontal shortening and subvertical principal stretch (Cochelin et al., 2017, 2018).

The partially molten mid-lower crust is observed in domes (Fig. 1a). The interpolated foliation trajectories, both at regional and local scales (see Figs. 7a & 13b), display circular to concentric trajectories within and around the domes. At regional scale, the ca. 15-20 km periodicity in the cleavage striking variations observed in the experimental variogram (Fig. 6a) shows that the domes display almost constant widths and could represent the periodical average map interdistance between them. We infer that this is related to a mechanical instability effect in the Variscan crust during original doming and exhumation of mid-lower crust. Smooth cleavage and lineation trajectories within gneiss domes (e.g. the Canigou massif) point to a rather homogeneous strainfield in the mid-lower crust with mainly longitudinal to slightly oblique stretching (Fig. 15) within domes' core.

Figure 15 here

In order to study the transitions from the upper crust to the mid-lower crust strains, one must consider the overall cleavage measurements dataset. At first glance, the nested structure of the regional-scale experimental variogram (Fig. 6a, grey dots/black curve) suggests that the Axial Zone includes distinct strainfields. Indeed, when considered separately, the cleavage measurements from the upper- and the mid-lower crust give two different variograms with distinct trends and parameters (Fig. 6a). Yet, if the two strain fields evidenced would display directions cross-cutting relationships (in particular within the contact/transition zones), the variogram computed for the overall data (in black, Fig. 6a) would display a significantly higher *nugget* value than the two others taken individually; which is not the case here. Besides, cleavage of the upper-crust has very steady orientations (i.e. both in strike and dip) and a dominant longitudinal collinear trend across the overall Axial Zone but some "disturbances" are linked to the gneiss domes. Thus, the finite strain orientation of upper-crust is dependent on the mid-lower crust fabric orientation when approaching domes' envelops, suggesting coeval deformation. While shallow parts of the Variscan crust of the Pyrenees was affected by homogeneous thickening, the mid-lower crust was contemporarily affected by homogeneous longitudinal stretching (Figs 11 & 15) reflecting lateral horizontal flow, which is also compatible with NS horizontal shortening. This suggests vertical coupling during deformation (Tikoff et al., 2002). As proposed by Cochelin et al. (2017), such a vertical strain partitioning is typical of hot and ultra-hot orogens, where lithosphere has been significantly weakened (Cagnard et al., 2006a,b, Cruden et al., 2006, Chardon et al., 2009).

When considering the overall cleavage direction dataset – including upper-crust, plutons and gneiss domes – the interpolated trajectory map underline a quite heterogeneous pattern, with

strain localization into regional scale, anastomosed longitudinal bands (Fig. 7a). These bands correspond to dextral-reverse shear zones observed in the field and mapped (e.g. Carreras, 2001; Cochelin et al., 2017). The localization of these anastomosed shear zones seems to be intimately linked to the emplacement of gneiss domes and syn-kinematics plutons, as shear zones border these massifs (Fig. 7a). Domes and plutons must have acted as regional heterogeneities while the crust was affected by NS horizontal shortening. Therefore, we consider that these regional shear zones nucleated because of the emplacement of domes and plutons – themselves driven by mechanical instability during regional-scale shortening. Such an interpretation is further supported by geochronological and field structural studies arguing that steep shear zones were activated during and after the emplacement of gneiss domes and plutons (Vilà et al., 2007; Denèle et al., 2007; 2009; Druguet et al., 2014; Cochelin et al., 2017; Van Lichtervelde et al., 2017).

At second order, directional-variograms computed for the upper-crust (Fig. 9a) document ~15-20km periodical undulations of the cleavage directions following a NE-SW spatial direction. Likewise, the corresponding interpolated trajectories display asymmetrical strain gradients (sigmoidal undulations) compatible with a dextral component of simple shear along few N120-140°E trending bands (Fig. 7a), which are characterized by domains of more shallowly plunging lineations (Fig. 11-left). Nevertheless, these bands appear poorly significant at regional scale as the trajectories are mostly collinear and symmetrical. Thus, these undulations reflect horizontal strain partitioning in response to the emplacement of local heterogeneities in a more homogeneous general strainfield. Therefore, our results show that the dextral shearing component of deformation has been over- stressed in previous studies because most of them were focused on syn-kinematic plutons, and had had a minor impact on the strainfield.

5.2. The variogram analysis, a tool to investigate the rheological behavior of the crust

As a preliminary step, the variogram calculation and analysis is critical to detect and quantify significant variations (including the maximum correlation distance, variance and behavior at short distances) of the studied *regionalized variable* as well as potential anisotropy. We propose hereafter that, whatever the scale considered, the best fitted trend of variograms can be used to characterize the rheological behavior or the tectonic history of the geological object/domain investigated.

Amplitude of the variations in the measured values is evaluated by the *sill* (general variations; variance) and the *nugget* values in an experimental variogram. On the other hand, whatever those variations, the behavior to the origin of the variograms allows quantifying the way the variable varies with distance. In this study, gaussian or sinusoidal variograms have been computed for structures such as syn-kinematic plutons and gneiss domes. The very low original slope of these variogram functions points to limited and very progressive variations between structural orientation measurements, as exemplified by the Mt-Louis pluton and the Canigou gneiss dome (Figs. 12a & 14b). Indeed, the Mt Louis pluton, displays highly continuous and progressive strain variations and non-localized simple shear corridors. As shearing of the pluton happened during its cooling (Bouchez & Gleizes, 1995), we argue that the trend of the corresponding variogram can be diagnostic of such homogeneous/continuous deformation through time in case of weak mechanical behavior such as cooling magmas (Fig. 16). Similarly, in the Canigou gneiss dome, stretching lineations formed during pervasive metamorphism and crustal flow show continuous and smooth variations in trends, as illustrated by a sinusoidal variogram (Fig. 14b). To us, this phenomenon may also reflect a continuous ductile deformation at high temperature, which remains undisturbed during late Variscan folding and post-Paleozoic faulting (Fig. 16).

Figure 16 here

Exponential or spherical variogram trends – with a significantly high original slope – correspond to a fast decorrelation between data point values with distance. We thus argue that geological objects or structural domains characterized by such variogram trends have experienced less homogeneous deformation or a polyphased tectonic history. Indeed, zooming on the Canigou dome shows that variations of cleavage directions are mainly disturbed by post-metamorphic structural discontinuities (i.e. faults). Such discontinuities may induce the modification of an initially sinusoidal or gaussian variogram trend – as witnessed by the lineations dataset – into a typically disturbed variogram (i.e. exponential trend), as illustrated in Figure 16. At regional scale, the cleavage orientations from the whole upper crust (metasediments) reflect interferences between a regional and consistent trend and the domes and plutons. For upper crust, the corresponding variogram clearly displays an exponential trend with a quite short *range* distance (Fig. 16). Domes and plutons can be regarded as geological discontinuities in the upper crust, explaining the exponential variogram trend for the upper crust dataset (Fig. 16) and the resulting interpolated trajectories showing local bending and reorientations around them (Fig. 10). Finally, the spherical trend of the omnidirectional-variogram that characterizes the whole Axial Zone reflects multi-scale interferences in a homogeneous strainfield recorded through time in the basement. This variogram corresponds to the imbrication, the convolution of all the variograms including local to regional variations induced by all the geological and structural objects/domains that compose the exposed crust (Fig. 16).

6. Concluding points

The present study shows that geostatistics is a powerful tool to model continuous strain trajectories from local ductile structure measurements. This inversion method can be considered

659 as alternative and complementary to forward analog or thermo-mechanical modelling to
660 investigate strainfields and the interplay of different mechanical controls leading to the
661 development of finite strain in the crust. In particular, this study shows that the approach
662 developed allows:

663 - Separating (i) significant local to regional variations in strainfields from (ii) variations
664 that cannot be considered and modeled from structural data. Variogram analysis allows
665 determining the spatial scale (maximum distance) of influence of the tectonic and/or
666 rheological controls on strain spatial variations. To the opposite, background noise or very
667 local variations are integrated to the nugget effect and not modeled in computed
668 trajectories for instance. At the scale of the Axial Zone of the Pyrenees, such non-
669 significant variations make ~50% of the total variance of the dataset.
670 - Investigating strainfields at different scales, from a same structural dataset. By separating
671 trends which are significant at a given scale from variations regarded as some noise or too
672 "local", different sub-scales can thus be explored within a study area. When zooming on
673 very local sub-domains, variations initially considered as "noise" in the regional-scale
674 nugget effect can become significant and be interpreted. In the case of the Pyrenean Axial
675 Zone, local interpolated map of the Canigou gneiss dome or Mt-Louis pluton display
676 more detailed trajectories than at regional-scale, where internal variations can be regarded
677 as irrelevant.
678 - Deconvoluting juxtaposed strainfields. Nested structures of experimental variograms
679 point out combined effects of different imbricated phenomena. The variogram analysis of
680 data sub-sets, for distinct structural domains, allows quantifying their relative impact on

the strainfield, which can be regarded as composed of multiple-signals of specific spatial range and structural significance.

- Revealing contrasted mechanical behaviors of lithological/structural domains. Indeed, results show that spatial strain gradients of structural domains can be evaluated from the trend of the corresponding variogram functions. Geostatistical analysis thus allows distinguishing pervasive *vs.* localized deformation regimes at a given scale. Besides, the original variogram trend can also point-out a role of late structures (faults in particular) forming discontinuities and perturbations in the paleo-strainfield.

Acknowledgments

This work was supported by the BRGM through the Référentiel Géologique de la France program (RGF). We warmly thank B. Bourgine (BRGM – France) for fruitful discussion about variogram analysis. We also thank two anonymous reviewers for helping to improve the manuscript and William Dunne for the editorial handling.

References

Aguilar, C., Liesa, M., Štípská, P., Schulmann, K., Muñoz, J.A., Casas, J.M., 2015. P–T–t–d evolution of orogenic middle crust of the Roc de Frausa Massif (Eastern Pyrenees): a result of horizontal crustal flow and Carboniferous doming? Journal of Metamorphic Geology 33, 273–294. https://doi.org/10.1111/jmg.12120

Angelier, J., 1984. Tectonic analysis of fault slip data sets. Journal of Geophysical Research: Solid Earth 89, 5835–5848. https://doi.org/10.1029/JB089iB07p05835

Aurejac, J.B., Gleizes, G., Diot, H., J.L., B., 2004. Le complexe granitique de Quérigut (Pyrénées, France) ré-examiné par la technique de l'ASM : un pluton syntectonique de la transpression dextre hercynienne. Bulletin de la Société Géologique de France 175, 157–174.

Baudin, T., Autran, A., Guitard, G., Laumonier, B., 2008. Carte géologique de la France (1/ 50.000), feuille Arles-sur-Tech (1100). BRGM, Orléans, France.

706 Blès, J.L., Bonijoly, D., Castaing, C., Gros, Y., 1989. Successive post-Variscan stress fields in the French
707 Massif Central and its borders (Western European plate): comparison with geodynamic data.
708 Tectonophysics 169, 79–111. https://doi.org/10.1016/0040-1951(89)90185-6

709 Bouchez, J.L., Gleizes, G., 1995. Two-stage deformation of the Mont-Louis-Andorra granite pluton
710 (Variscan Pyrenees) inferred from magnetic susceptibility anisotropy. Journal of the Geological Society
711 152, 669–679. https://doi.org/10.1144/gsjgs.152.4.0669

712 Branquet, Y., Gumiaux, C., Sizaret, S., Barbanson, L., Wang, B., Cluzel, D., Li, G., Delaunay, A., 2012.
713 Synkinematic mafic/ultramafic sheeted intrusions: Emplacement mechanism and strain restoration of the
714 Permian Huangshan Ni–Cu ore belt (Eastern Tianshan, NW China). Journal of Asian Earth Sciences 56,
715 240–257. https://doi.org/10.1016/j.jseaes.2012.05.021

716 Brun, J.-P., 1983. L'origine des dômes gneissiques: modèles et tests. Bulletin de La Société Géologique de
717 France 7, XXV (2), 219–228.

718 Brun, J.-P., 2002. Deformation of the continental lithosphere: Insights from brittle-ductile models.
719 Geological Society, London, Special Publications 200, 355–370.
720 https://doi.org/10.1144/GSL.SP.2001.200.01.20

721 Brun, J.-P., Pons, J., 1981. Strain patterns of pluton emplacement in a crust undergoing non-coaxial
722 deformation, Sierra Morena, Southern Spain. Journal of Structural Geology 3, 219–229.
723 https://doi.org/10.1016/0191-8141(81)90018-3

724 Cagnard, F., Durrieu, N., Gapais, D., Brun, J.-P., Ehlers, C., 2006a. Crustal thickening and lateral flow
725 during compression of hot lithospheres, with particular reference to Precambrian times. Terra Nova 18,
726 72–78. https://doi.org/10.1111/j.1365-3121.2005.00665.x

727 Cagnard, F., Brun, J.-P., Gapais, D., 2006b. Modes of thickening of analogue weak lithospheres.
728 Tectonophysics 421, 145–160. https://doi.org/10.1016/j.tecto.2006.04.016

729 Calais, E., Nocquet, J.-M., Jouanne, F., Tardy, M., 2002. Current strain regime in the Western Alps from
730 continuous Global Positioning System measurements, 1996–2001. Geology 30, 651–654.
731 https://doi.org/10.1130/0091-7613(2002)030<0651:CSRITW>2.0.CO;2

732 Carrara, A., Cardinali, M., Detti, R., Guzzetti, F., Pasqui, V., Reichenbach, P., 1991. GIS techniques and
733 statistical models in evaluating landslide hazard. Earth Surface Processes and Landforms 16, 427–445.
734 https://doi.org/10.1002/esp.3290160505

735 Carreras, J., 2001. Zooming on Northern Cap de Creus shear zones. Journal of Structural Geology 23,
736 1457–1486. https://doi.org/10.1016/S0191-8141(01)00011-6

737 Carreras, J., Capella, I., 1994. Structures and Tectonics at Different Lithospheric Levels Tectonic levels in
738 the Palaeozoic basement of the Pyrenees: a review and a new interpretation. Journal of Structural Geology
739 16, 1509–1524. https://doi.org/10.1016/0191-8141(94)90029-9

740 Carreras, J., Debat, P., 1996. Tectonique Hercynienne. In Synthèse Géologique et Géophysique Des
741 Pyrénées vol. 1. BRGM-ITGE, Orléans, France, pp. 501–584.

742 Carreras, J., Druguet, E., 2014. Framing the tectonic regime of the NE Iberian Variscan segment.
743 Geological Society, London, Special Publications 405, 249–264. https://doi.org/10.1144/SP405.7

744 Casas, J.M., Castiñeiras, P., Navidad, M., Liesa, M., Carreras, J., 2010. New insights into the Late
745 Ordovician magmatism in the Eastern Pyrenees: U–Pb SHRIMP zircon data from the Canigó massif.
746 Gondwana Research 17, 317–324. https://doi.org/10.1016/j.gr.2009.10.006

747 Chardon, D., Gapais, D., Cagnard, F., 2009. Flow of ultra-hot orogens: A view from the Precambrian,
748 clues for the Phanerozoic. Tectonophysics 477, 105–118. https://doi.org/10.1016/j.tecto.2009.03.008

749 Choukroune, P., 1992. Tectonic evolution of the Pyrenees. Annual Review of Earth and Planetary
750 Sciences 20, 143–158.

751 Choukroune, P., Bouhallier, H., Arndt, N.T., 1995. Soft lithosphere during periods of Archaean crustal
752 growth or crustal reworking. Geological Society, London, Special Publications 95, 67–86.
753 https://doi.org/10.1144/GSL.SP.1995.095.01.05

754 Chown, E.H., Daigneault, R., Mueller, W., Mortensen, J.K., 1992. Tectonic evolution of the Northern
755 Volcanic Zone, Abitibi belt, Quebec. Canadian Journal of Earth Sciences 29, 2211–2225.
756 https://doi.org/10.1139/e92-175

757 Cobbold, P.R., Barbotin, E., 1988. The geometrical significance of strain trajectory curvature. Journal of
758 Structural Geology 10, 211–218. https://doi.org/10.1016/0191-8141(88)90118-6

759 Cochelin, B., Chardon, D., Denèle, Y., Gumiaux, C., Le Bayon, B., 2017. Vertical strain partitioning in
760 hot Variscan crust: Syn-convergence escape of the Pyrenees in the Iberian-Armorican syntax. Bulletin de
761 La Société Géologique de France 188, 39. https://doi.org/10.1051/bsgf/2017206

762 Cochelin, B., Lemirre, B., Denèle, Y., Blanquat, M. de S., Lahfid, A., Duchêne, S., 2018. Structural
763 inheritance in the Central Pyrenees: the Variscan to Alpine tectonometamorphic evolution of the Axial
764 Zone. Journal of the Geological Society 175, 336-351. https://doi.org/10.1144/jgs2017-066

765 Cruden, A.R., Nasseri, M.H.B., Pysklywec, R., 2006. Surface topography and internal strain variation in
766 wide hot orogens from three-dimensional analogue and two-dimensional numerical vice models.
767 Geological Society, London, Special Publications 253, 79–104.
768 https://doi.org/10.1144/GSL.SP.2006.253.01.04

769 Davis, J.R. and S.J., Titus, 2017. Modern methods of analysis for three-dimensional orientational data,

770 Journal of Structural Geology 96, pp. 65–89. https://doi.org/10.1016/j.jsg.2017.01.002.

771 Davy, P., 1986. Modélisation thermo-mécanique de la collision continentale. PhD thesis, University of
772 Paris XI, Orsay, France, 200pp.

773 Debon, F., Enrique, P., Autran, A., 1996. Magmatisme hercynien. In Synthèse Géologique et Géophysique
774 Des Pyrénées vol. 1. BRGM-ITGE, Orléans, France, pp. 361–499.

775 Denèle, Y., Olivier, P., Gleizes, G., Barbey, P., 2007. The Hospitalet gneiss dome (Pyrenees) revisited:
776 lateral flow during Variscan transpression in the middle crust. Terra Nova 19, Pages 445-453.
777 https://doi.org/10.1111/j.1365-3121.2007.00770.x

778 Denèle, Y., Olivier, P., Gleizes, G., 2008. Progressive deformation of a zone of magma transfer in a
779 transpressional regime: The Variscan Mérens shear zone (Pyrenees, France). Journal of Structural
780 Geology 30, 1138–1149. https://doi.org/10.1016/j.jsg.2008.05.006

781 Denèle, Y., Olivier, P., Gleizes, G., Barbey, P., 2009. Decoupling between the middle and upper crust
782 during transpression-related lateral flow: Variscan evolution of the Aston gneiss dome (Pyrenees, France).
783 Tectonophysics 477, 244–261. https://doi.org/10.1016/j.tecto.2009.04.033

784 Denèle, Y., Laumonier, B., Paquette, J.-L., Olivier, P., Gleizes, G., Barbey, P., 2014. Timing of granite
785 emplacement, crustal flow and gneiss dome formation in the Variscan segment of the Pyrenees.
786 Geological Society, London, Special Publications 405, 265–287. https://doi.org/10.1144/SP405.5

787 Donzeau, M., Laumonier, B., Guitard, G., Autran, A., Llac, F., Baudin, T., Calvet, M., 2010. Carte
788 géologique de la France (1/ 50.000), feuille Céret (1096), BRGM, Orléans, France.

789 Druguet, E., Castro, A., Chichorro, M., Pereira, M.F., Fernández, C., 2014. Zircon geochronology of
790 intrusive rocks from Cap de Creus, Eastern Pyrenees. Geological Magazine 151, 1095–1114.
791 https://doi.org/10.1017/S0016756814000041

792 Engdahl, E.R., Villasenor, J., 2002. Global seismicity: 1900–1999. In: Lee, W., et al. (Ed.), International
793 Handbook of Earthquake and Engineering Seismology. Amsterdam, The Netherlands, 655–690.

794 Escuder Viruete, J., Carbonell, R., Martí, D., Pérez-Estaún, A., 2003. 3-D stochastic modeling and
795 simulation of fault zones in the Albalá granitic pluton, SW Iberian Variscan Massif. Journal of Structural
796 Geology 25, 1487–1506. https://doi.org/10.1016/S0191-8141(02)00183-9

797 Gautier, P., Brun, J.-P., 1994. Crustal-scale geometry and kinematics of late-orogenic extension in the
798 central Aegean (Cyclades and Ewia Island). Tectonophysics 238, 399–424. https://doi.org/10.1016/0040-
799 1951(94)90066-3

800 Gleizes, G., Leblanc, D., Bouchez, J.L., 1998. The main phase of the Hercynian orogeny in the Pyrenees
801 is a dextral transpression. Geological Society, London, Special Publications 135, 267–273.
802 https://doi.org/10.1144/GSL.SP.1998.135.01.17

803 Grenerczy, G., Kenyeres, A., Fejes, I., 2000. Present crustal movement and strain distribution in Central
804 Europe inferred from GPS measurements. Journal of Geophysical Research: Solid Earth 105, 21835–
805 21846. https://doi.org/10.1029/2000JB900127

806 Grose, L., Laurent, G., Aillères, L., Armit, R., Jessell, M., Caumon, G., 2017. Structural data constraints
807 for implicit modeling of folds. Journal of Structural Geology 104, 80–92.
808 https://doi.org/10.1016/j.jsg.2017.09.013

809 Guitard, G., 1960. Linéations, schistosité et phases de plissement durant l'orogenèse hercynienne dans les
810 terrains anciens des Pyrénées orientales, leurs relations avec le métamorphisme et la granitisation [with
811 discussion]. Bulletin de La Société Géologique de France S7–II, 862–887.
812 https://doi.org/10.2113/gssgfbull.S7-II.7.862

813 Guitard, G., Geyssant, J., Laumonier, B., Autran, A., Fonteilles, M., Dalmayrach, B., Vidal, J.-C.,
814 Mattauer, M., Bandet, Y., 1992. Carte géologique de la France (1/ 50.000), feuille Prades (1095). BRGM,
815 Orléans, France.

816 Guitard, G., Vielzeuf, D., Martinez, F., 1996. Métamorphisme hercynien. In Synthèse Géologique et
817 Géophysique Des Pyrénées vol. 1. BRGM - ITGE, Orléans, France, pp. 501–584.

Gumiaux, C., Gapais, D., Brun, J.-P., 2003. Geostatistics applied to best-fit interpolation of orientation data. Tectonophysics 376, 241–259. https://doi.org/10.1016/j.tecto.2003.08.008

Gumiaux, C., Brun, J.-P., Gapais, D., 2004. Strain removal within the Hercynian Shear Belt of Central Brittany (western France): methodology and tectonic implications. Geological Society, London, Special Publications 224, 287–305. https://doi.org/10.1144/GSL.SP.2004.224.01.18

Hanke, J.R., Fischer, M.P., Pollyea, R.M., 2017. Directional semivariogram analysis to identify and rank controls on the spatial variability of fracture networks. Journal of Structural Geology 108, 34–51. https://doi.org/10.1016/j.jsg.2017.11.012

Hillier, M., de Kemp, E., Schetselaar, E., 2013. 3D form line construction by structural field interpolation (SFI) of geologic strike and dip observations. Journal of Structural Geology 51, 167–179. https://doi.org/10.1016/j.jsg.2013.01.012

Kahle, H.-G., Cocard, M., Peter, Y., Geiger, A., Reilinger, R., McClusky, S., King, R., Barka, A., Veis, G., 1999. The GPS strain rate field in the Aegean Sea and western Anatolia. Geophysical Research Letters 26, 2513–2516. https://doi.org/10.1029/1999GL900403

Koike, K., Kubo, T., Liu, C., Masoud, A., Amano, K., Kurihara, A., Matsuoka, T., Lanyon, B., 2015. 3D geostatistical modeling of fracture system in a granitic massif to characterize hydraulic properties and fracture distribution. Tectonophysics 660, 1–16. https://doi.org/10.1016/j.tecto.2015.06.008

Lacombe, O., Mouthereau, F., 2002. Basement-involved shortening and deep detachment tectonics in forelands of orogens: Insights from recent collision belts (Taiwan, Western Alps, Pyrenees). Tectonics 21, 12–1. https://doi.org/10.1029/2001TC901018

Martínez, F.J., Iriondo, A., Dietsch, C., Aleinikoff, J.N., Peucat, J.J., Cirès, J., Reche, J., Capdevila, R., 2011. U-Pb SHRIMP-RG zircon ages and Nd signature of lower Paleozoic rifting-related magmatism in the Variscan basement of the Eastern Pyrenees. Lithos 127, 10–23. https://doi.org/10.1016/j.lithos.2011.08.004

Matheron, G., 1962. Traité de Géostatistique Appliquée, Technip, Paris, 333 pp.

McKenzie, D., 1972. Active Tectonics of the Mediterranean Region. Geophysical Journal International 30, 109–185. https://doi.org/10.1111/j.1365-246X.1972.tb02351.x

Mezger, J.E., 2009. Transpressional tectonic setting during the main Variscan deformation: evidence from four structural levels in the Bossòst and Aston-Hospitalet mantled gneiss domes, central Axial Zone,

Pyrenees. Bulletin de la Société Géologique de France 180, 199–207. https://doi.org/10.2113/gssgfbull.180.3.199

Mezger, J.E., Passchier, C.W., 2003. Polymetamorphism and ductile deformation of staurolite–cordierite schist of the Bossòst dome: indication for Variscan extension in the Axial Zone of the central Pyrenees. Geological Magazine 140, 595–612. https://doi.org/10.1017/S0016756803008112

Rafiee, A., Vinches, M., 2008. Application of geostatistical characteristics of rock mass fracture systems in 3D model generation. International Journal of Rock Mechanics and Mining Sciences 4, 644–652. https://doi.org/10.1016/j.ijrmms.2007.09.009

Ramsay, J.G., 1967. Folding and Fracturing of Rocks, McGraw-Hill. New York.

Ramsay, J.G., Graham, R.H., 1970. Strain variation in shear belts. Canadian Journal of Earth Sciences 7, 786–813. https://doi.org/10.1139/e70-078

Riller, U., Clark, M.D., Daxberger, H., Doman, D., Lenauer, I., Plath, S., Santimano, T., 2017. Fault-slip inversions: Their importance in terms of strain, heterogeneity, and kinematics of brittle deformation. Journal of Structural Geology 101, 80–95. https://doi.org/10.1016/j.jsg.2017.06.013

Siddans, A.W.B., 1972. Slaty cleavage — a review of research since 1815. Earth-Science Reviews 8, 205–232. https://doi.org/10.1016/0012-8252(72)90084-0

de Sitter, L.U., Zwart, H.J., 1960. Tectonic development in supra and infra-structures of a mountain chain. Proceedings of the 21st International Geological Congress of Cophenhagen 18, 248–256.

Soliva, J., Salel, J.F., Brunnel, M., 1989. Shear deformation and emplacement of the gneissic Canigou thrust nappe (Eastern Pyrenees). Geologie En Mijnbouw 68, 357–388.

Soula, J.C., Debat, P., Deramond, J., Pouget, P., 1986. A dynamic model of the structural evolution of the Hercynian Pyrenees. Tectonophysics 129, 29–51.

Teyssier, C., Tikoff, B., 1999. Fabric stability in oblique convergence and divergence. Journal of Structural Geology 21, 969–974.

Tikoff, B., Greene, D., 1997. Stretching lineations in transpressional shear zones: an example from the Sierra Nevada Batholith, California. Journal of Structural Geology 19, 29–39.

Tikoff, B., Teyssier, C., Waters, C., 2002. Clutch tectonics and the partial attachment of lithospheric layers. EGU Stephan Mueller Special Publication Series 1, 57–73.

Titus, S.J., Dyson, M., DeMets, C., Tikoff, B., Rolandone, F., Bürgmann, R., 2011. Geologic versus geodetic deformation adjacent to the San Andreas fault, central California. GSA Bulletin 123, 794–820. https://doi.org/10.1130/B30150.1

Upton, G.J.G., Fingleton, B., 1989. Spatial Data Analysis by Example, vol. 2. Wiley, New York, 416 pp.

Van den Eeckhout, B., 1986. A case study of a mantled gneiss antiform, the Hospitalet massif, Pyrenees (Andorra, France). Geologica Ultraiectina 45, 1–189.

Van den Eeckhout, B., Zwart, H.J., 1988. Hercynian crustal-scale extensional shear zone in the Pyrenees. Geology 16, 135–138. https://doi.org/10.1130/0091-7613(1988)016<0135:HCSESZ>2.3.CO;2

Van Lichtervelde, M., Grand'Homme, A., Saint-Blanquat, M. de, Olivier, P., Gerdes, A., Paquette, J.-L., Melgarejo, J.C., Druguet, E., Alfonso, P., 2017. U-Pb geochronology on zircon and columbite-group minerals of the Cap de Creus pegmatites, NE Spain. Mineralogy and Petrology 111, 1–21. https://doi.org/10.1007/s00710-016-0455-1

Vilà, M., Pin, C., Liesa, M., Enrique, P., 2007. LP-HT metamorphism in a late orogenic transpressional setting, Albera Massif, NE Iberia: implications for the geodynamic evolution of the Variscan Pyrenees. Journal of Metamorphic Geology 25, 321–347. https://doi.org/10.1111/j.1525-1314.2007.00698.x

Welsch, W.M., 1983. Finite element analysis of strain patterns from geodetic observations across a plate margin. Tectonophysics, Recent Crustal Movements, 1982 97, 57–71. https://doi.org/10.1016/0040-1951(83)90125-7

Wood, D.S., 1974. Current Views of the Development of Slaty Cleavage. Annual Review of Earth and Planetary Sciences 2, 369–401. https://doi.org/10.1146/annurev.ea.02.050174.002101

Zhang, P.-Z., Shen, Z., Wang, M., Gan, W., Bürgmann, R., Molnar, P., Wang, Q., Niu, Z., Sun, J., Wu, J., Hanrong, S., Xinzhao, Y., 2004. Continuous deformation of the Tibetan Plateau from global positioning system data. Geology 32, 809–812. https://doi.org/10.1130/G20554.1

Zwart, H.J., 1979. The geology of the Central Pyrenees. Leidse Geol. Mededelingen 50, 1–74.

Zwart, H.J., 1986. The variscan geology of the Pyrenees. Tectonophysics 129, 9–27. https://doi.org/10.1016/0040-1951(86)90243-X

Figure captions

Figure 1: a) Sketch map of the Paleozoic crust of the Pyrenees. The plutons and gneiss domes cited in the text are located. Location of the two cross-sections of Figs. 1b & 1c and Fig. 2 are also shown. Abbreviation for west to east: Ct: Cauterets pluton, CL: Chiroulet-Lesponne dome, Nv: Néouvielle pluton, LC: Lys-Caillaouas dome, Bo: Bossost dome, Ma: Maladeta pluton, Ba: Bassiès pluton, As: Aston gneiss dome, Ho: Hospitalet gneiss dome, ML: Mt Louis pluton, Qt: Quérigut pluton, Mi: Millas pluton, Ca: Canigou gneiss dome, Ab: Albères gneiss dome. In dark-grey: main Variscan shear zones; in blue: main Alpine faults; b) Simplified cross-section from the central Axial Zone, modified from Cochelin et al., 2018; c) simplified cross-section from the eastern Pyrenees, modified from Cochelin et al., 2017

Figure 2: Simplified geological map of the Canigou gneiss dome, modified from Guitard et al., (1992) Carreras et al., (2004); Baudin et al., (2008); Donzeau et al., (2010).

Figure 3: Summary of the following steps to compute foliation trajectories. See in the text for further explanation.

Figure 4: Summary of the following steps to compute lineation trajectories, using lineation data set presented in Fig. 3.

Figure 5: a) Histogram of cleavage directional data, b) histogram of cleavage directional data in the upper crust; c) histogram of foliation directional data in the middle crust. The calculated skewness for each histogram corresponds to the nonparametric skew. Rose diagrams of dip values of cleavage/foliation planes in the Axial Zone (d), the middle crust (e) and the upper crust (f).

Figure 6: a) Omni-directional variograms computed for schistosity directional data, with the omni-directional variograms computed for the whole Axial Zone in black, the upper crust in blue

925 and the mid-lower crust in red. Dots represent the experimental variograms and full lines are the
926 fest-fit functions; b) Omni-directional variograms of dip values for the Axial Zone (black) and
927 the upper crust (blue).

928 Figure 7: a) Cleavage trend trajectories computed from the interpolated cleavage direction in the
929 whole Axial Zone, taking into account gneiss domes and plutons; b) R map computed from the
930 interpolated cleavage direction. High dispersion is highlighted by low R values in orange and red.

931 Figure 8: a) Interpolated dip of cleavage in the Axial Zone. Gneiss domes are located in red and
932 plutons in black. b) Computed slope of dip values in the Axial Zone. Sharp variations are
933 highlighted by high slopes in red (0.83 to 2.26%) and beige (0.45-0.82%).

934 Figure 9: Directional variograms computed in the upper crust: a) for azimuth of cleavage along
935 the N45° direction in the upper crust; b) for azimuth of cleavage along EW, NW-SE and NS
936 directions in the upper crust. c) N100° directed variogram computed for dip values in the upper
937 crust. d) N10° directed variogram computed for dip values in the upper crust.

938 Figure 10: a) Cleavage trend trajectories computed from the interpolated cleavage direction in the
939 upper crust; b) Interpolated dip of cleavage in the upper crust. These interpolations were obtained
940 using nugget effect and ranges deduced from the variogram analysis of the upper crust (Fig.6a).

941 Figure 11: Ternary diagrams (Pitch-Plunge-Dip) illustrating the crustal flow mode in orogens,
942 after Chardon et al., (2009) for mineral-stretching lineations in the upper crust (left) and the mid-
943 lower crust (right) of the Variscan Pyrenees. Because the association of foliation and lineation in
944 each station was not possible for digitalized data, those presented in this figure come from our
945 own measurement (see Cochelin et al., 2017).

946 Figure 12: a) Omni-directional variogram computed for directional data in the Mt Louis pluton;
947 b) Zoom on the regional trajectories obtained around the Mt Louis pluton (Fig. 7a); c) Foliation
948 trajectories obtained using parameters deduced from the omni-directional variogram of the
949 pluton; d) Foliation trajectories obtained manually by Bouchez and Gleizes (1995) on the basis of
950 ASM measurement and field observations.

951 Figure 13: Zoom on the Canigou gneiss dome. a) Omni-directional variogram calculated for
952 foliation planes within the gneiss dome; b) Local foliation trajectories in the Canigou gneiss
953 dome (in red); Trajectories around the gneiss dome (in grey) are from the regional interpolation
954 (Fig. 7a). c) Location of high dispersion of directional data in the Canigou gneiss dome
955 combining of zoom of the R map (Fig. 7b), local trajectories (Fig. 13b) and location of the main
956 fault zones (Fig. 2).

957 Figure 14: a) Stereogram of mineral-stretching lineations in the Canigou gneiss dome; b) Omni-
958 directional variogram computed for stretching lineations; c) Computed lineation trajectories in
959 the Canigou gneiss dome.

960 Figure 15: a) Synthesis of direction of stretching within gneiss domes in the Axial Zone,
961 modified from Cochelin et al., 2017; b) Rose diagram of mineral-stretching lineations set
962 available for gneiss domes

963 Figure 16: Bloc diagram summarizing how strain was spatially partitioned in the Axial Zone,
964 showing: the steep longitudinal cleavage trajectories in the upper crust (1) and associated
965 transpressional shear zones in blue surrounding syn-kinematic plutons (2) and gneiss domes (3)
966 affected by longitudinal stretching. The simplified trend of variograms for each structural features
967 is presented: the nested variogram of the Axial Zone, summing the individual variograms of (1)

968 the upper crust with its exponential trend; (2) syntectonic plutons showing sinusoidal trend; (3)
969 gneiss domes which could have a sinusoidal trend (i.e. single phased or “undisturbed” domes) or
970 an exponential trend (i.e. polyphased domes like the Canigou).

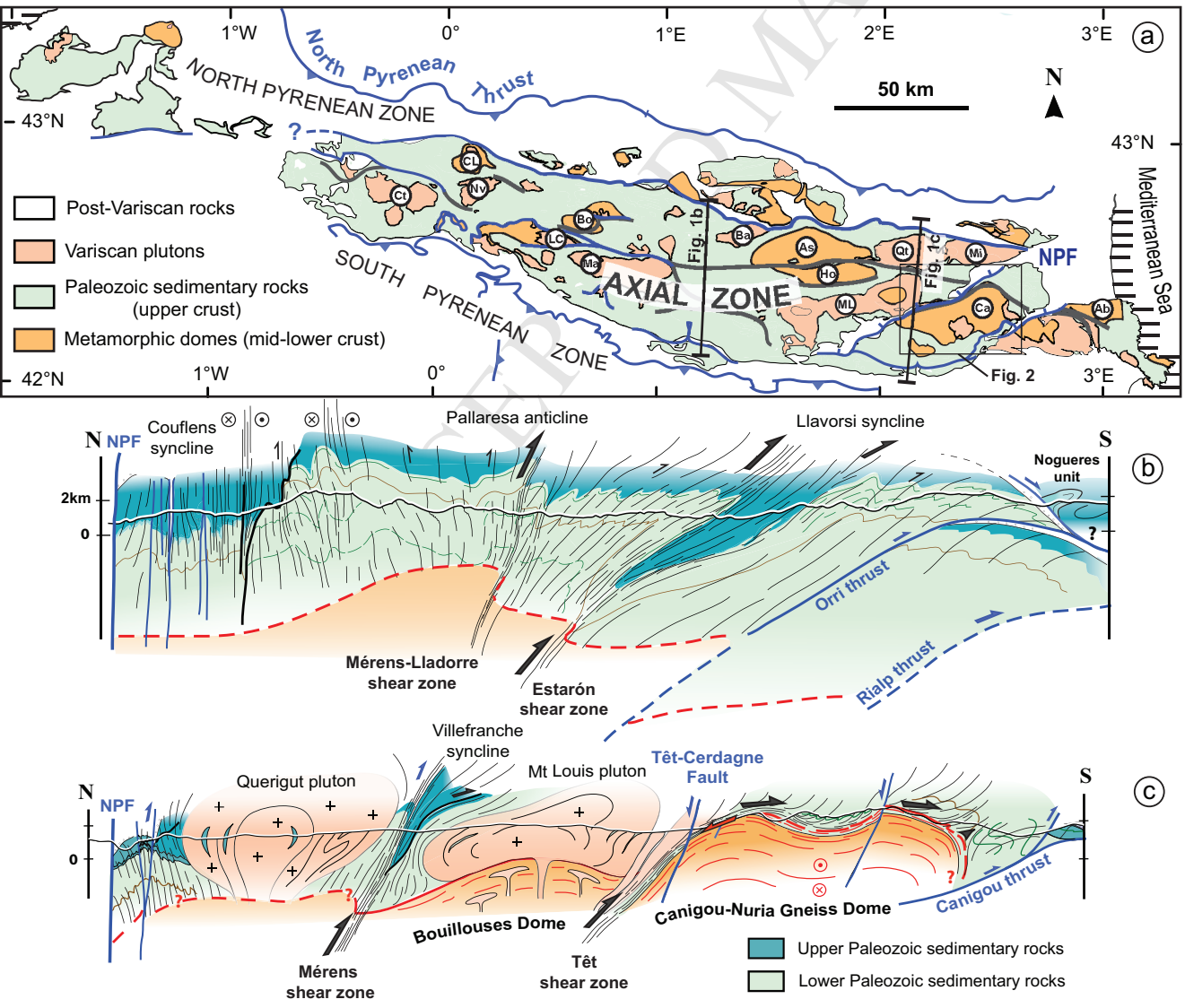

Cochelin et al. Figure 1

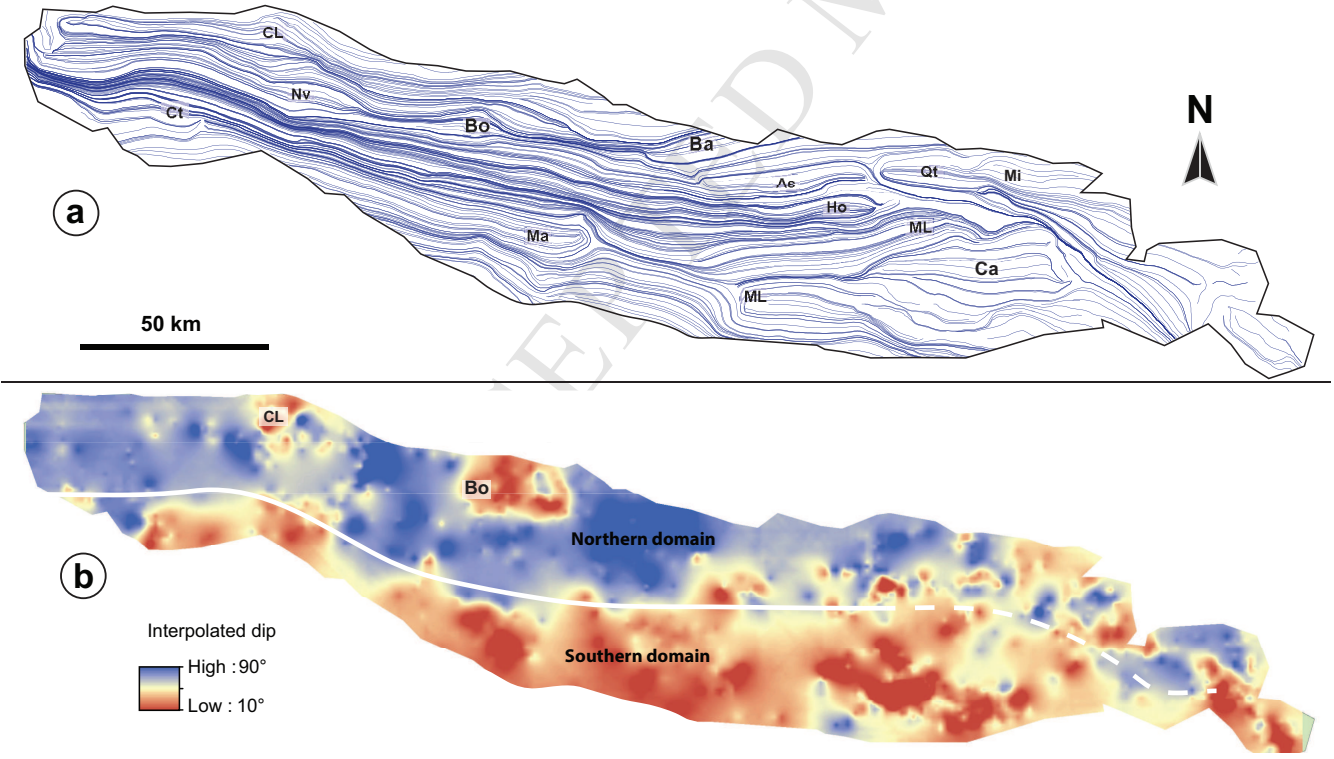

Cochelin et al., Figure 10

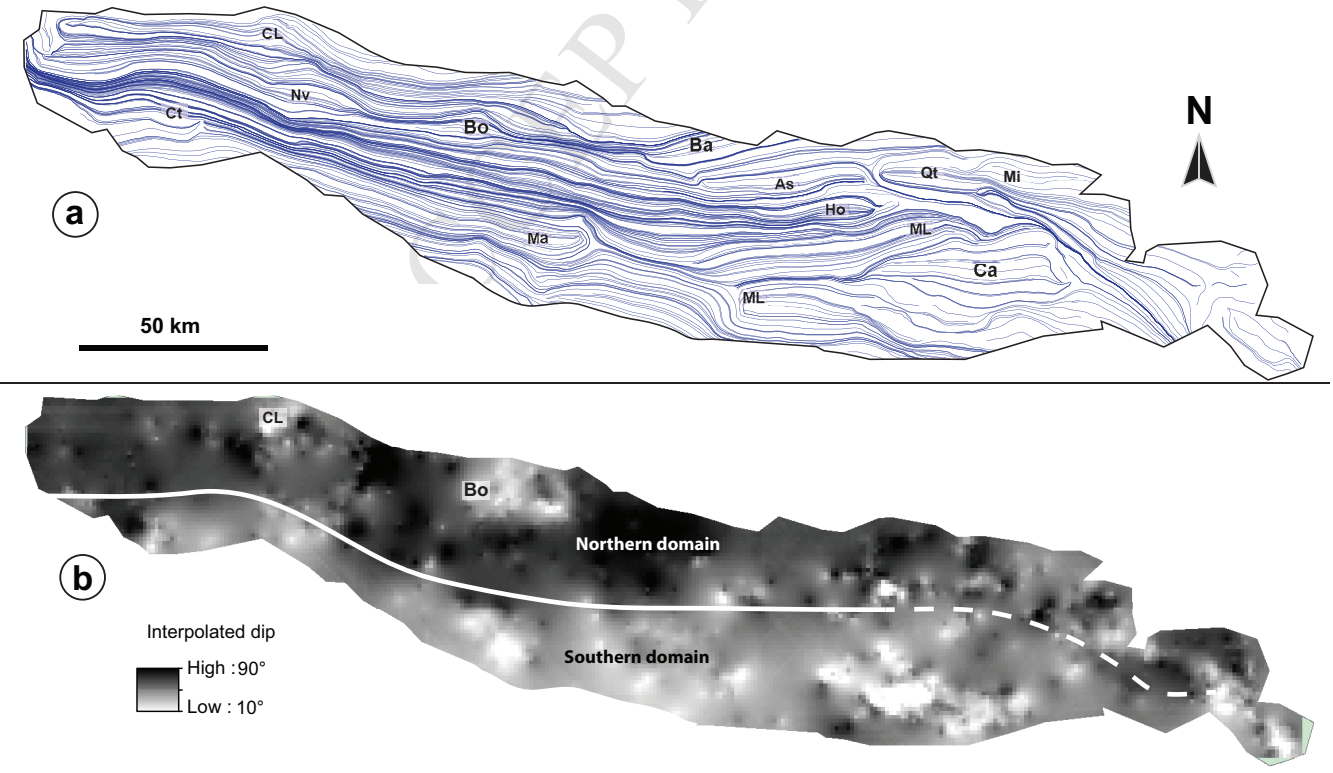

Cochelin et al., Figure 10

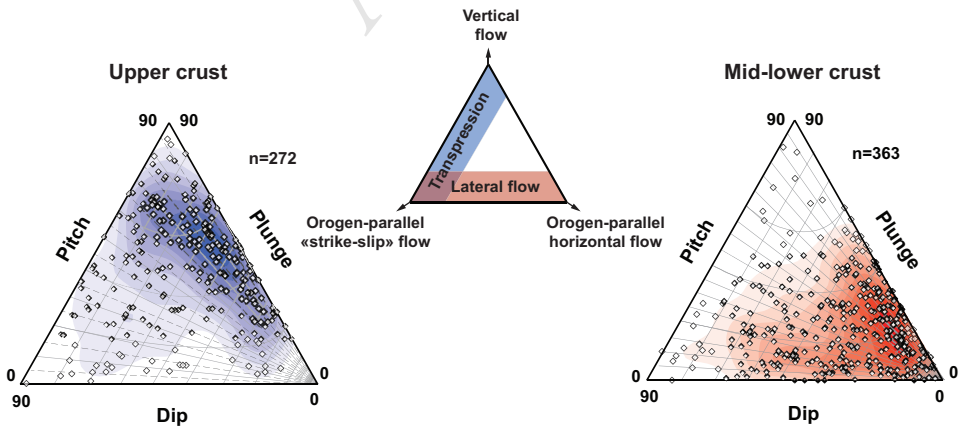

Cochelin et al., Figure 11

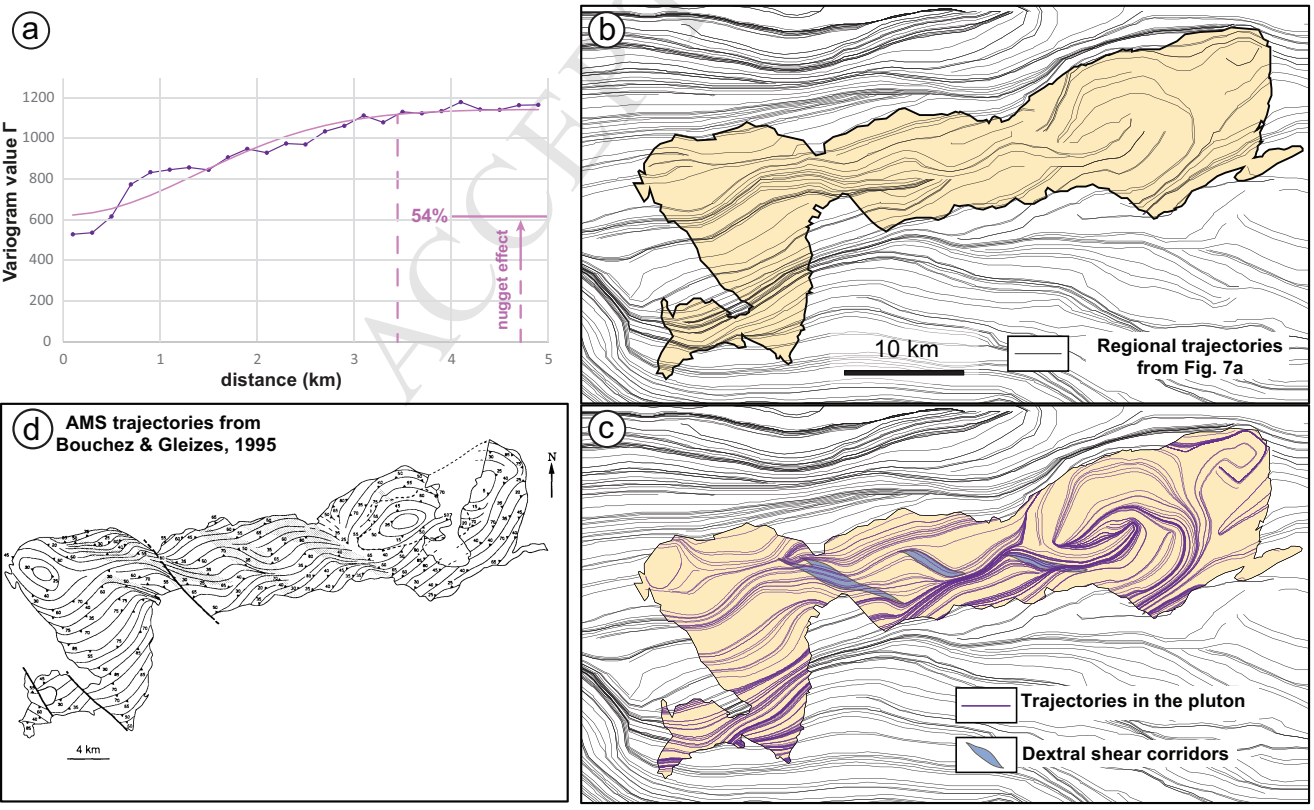

Cochelin et al. Figure 12

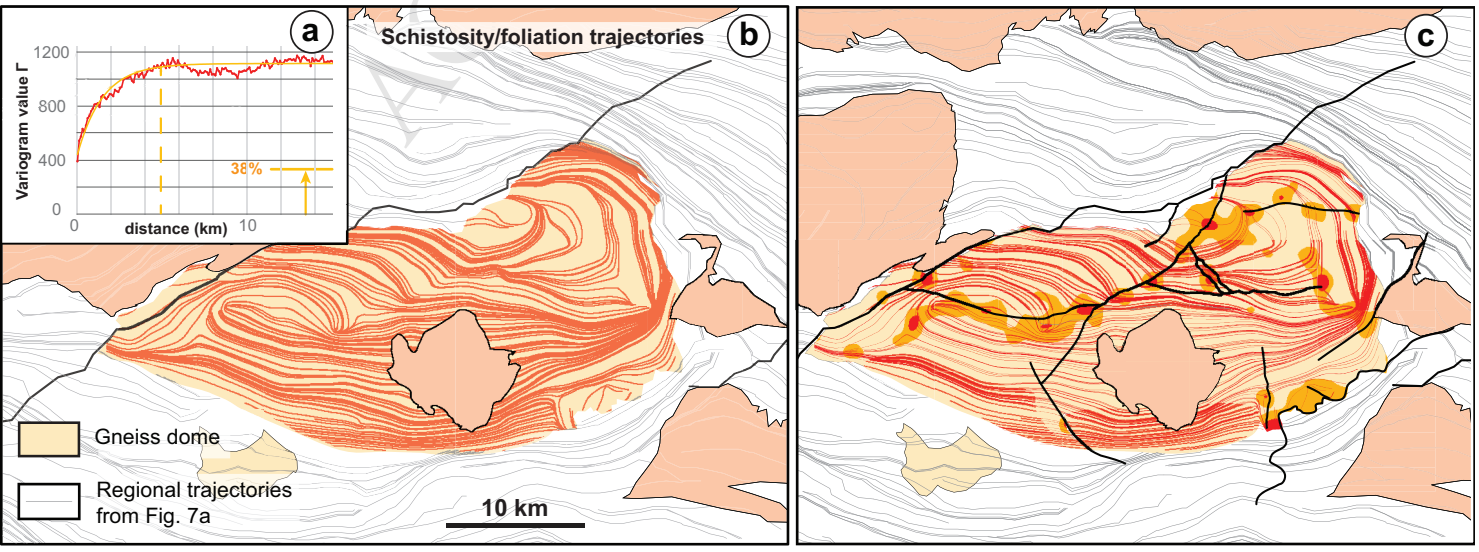

Cochelin et al. Figure 13

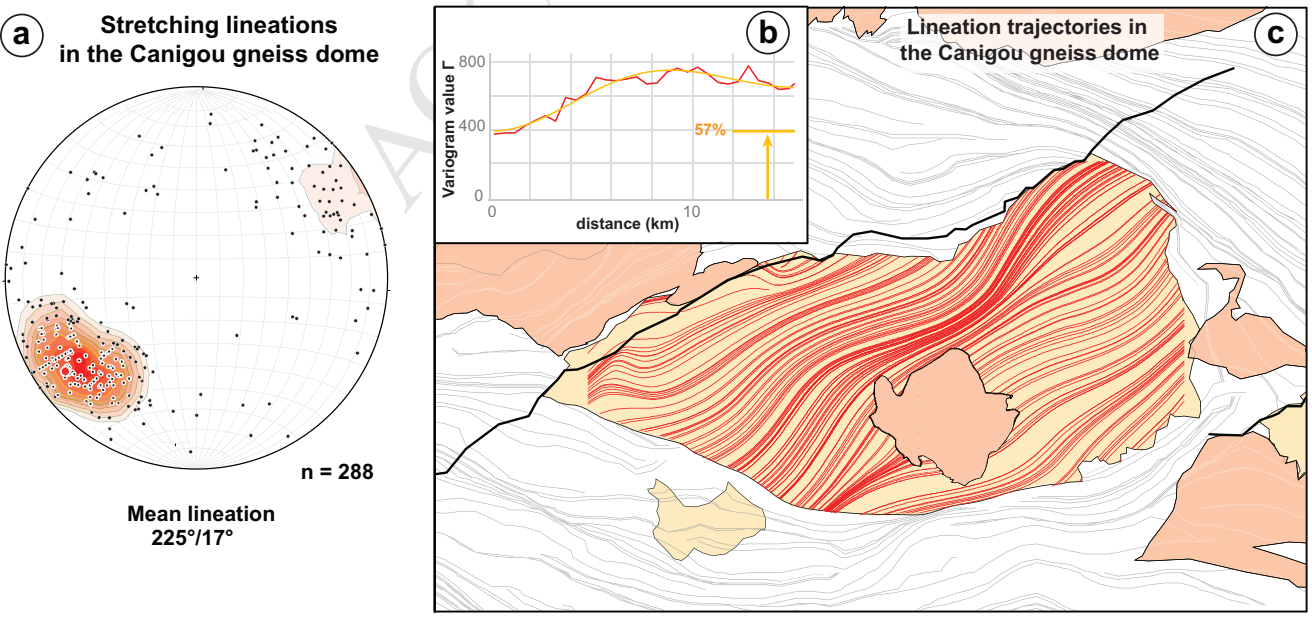

Cochelin et al., Figure 14

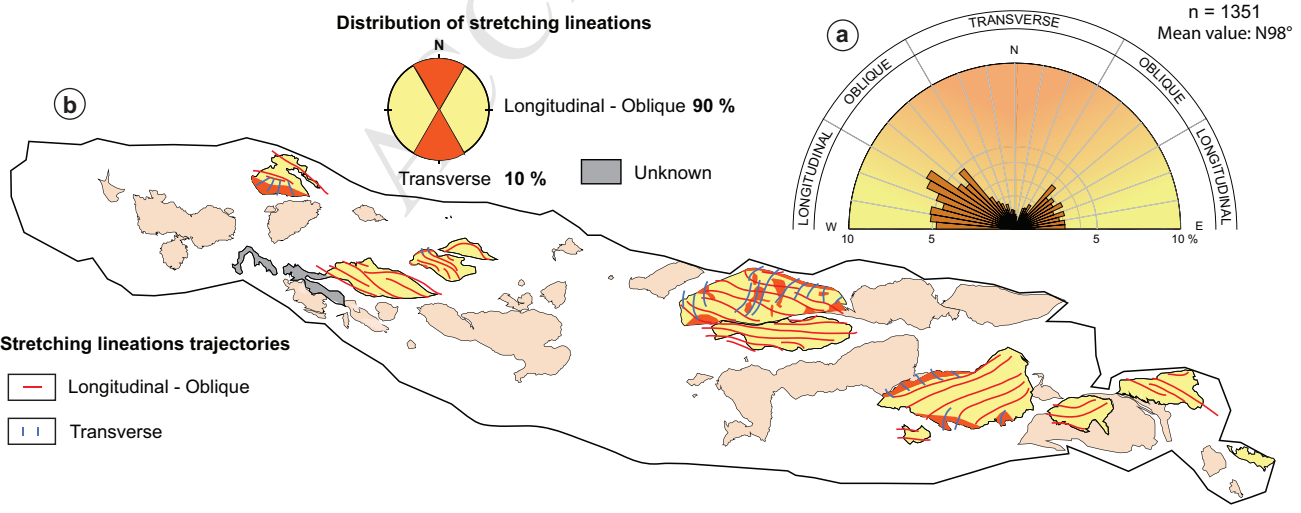

Cochelin et al. Figure 15

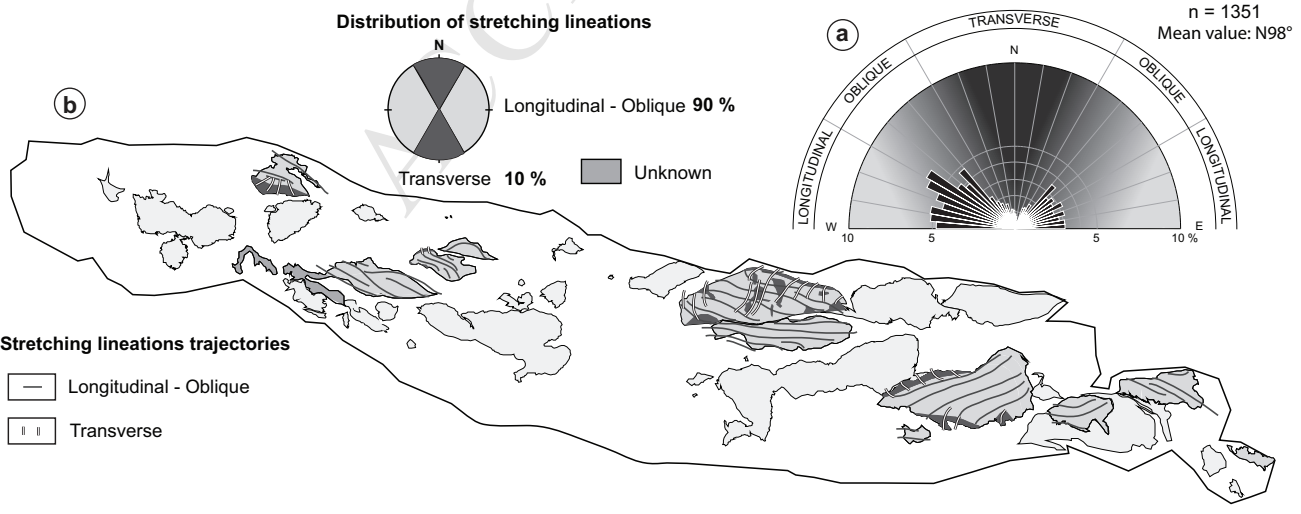

Cochelin et al. Figure 15

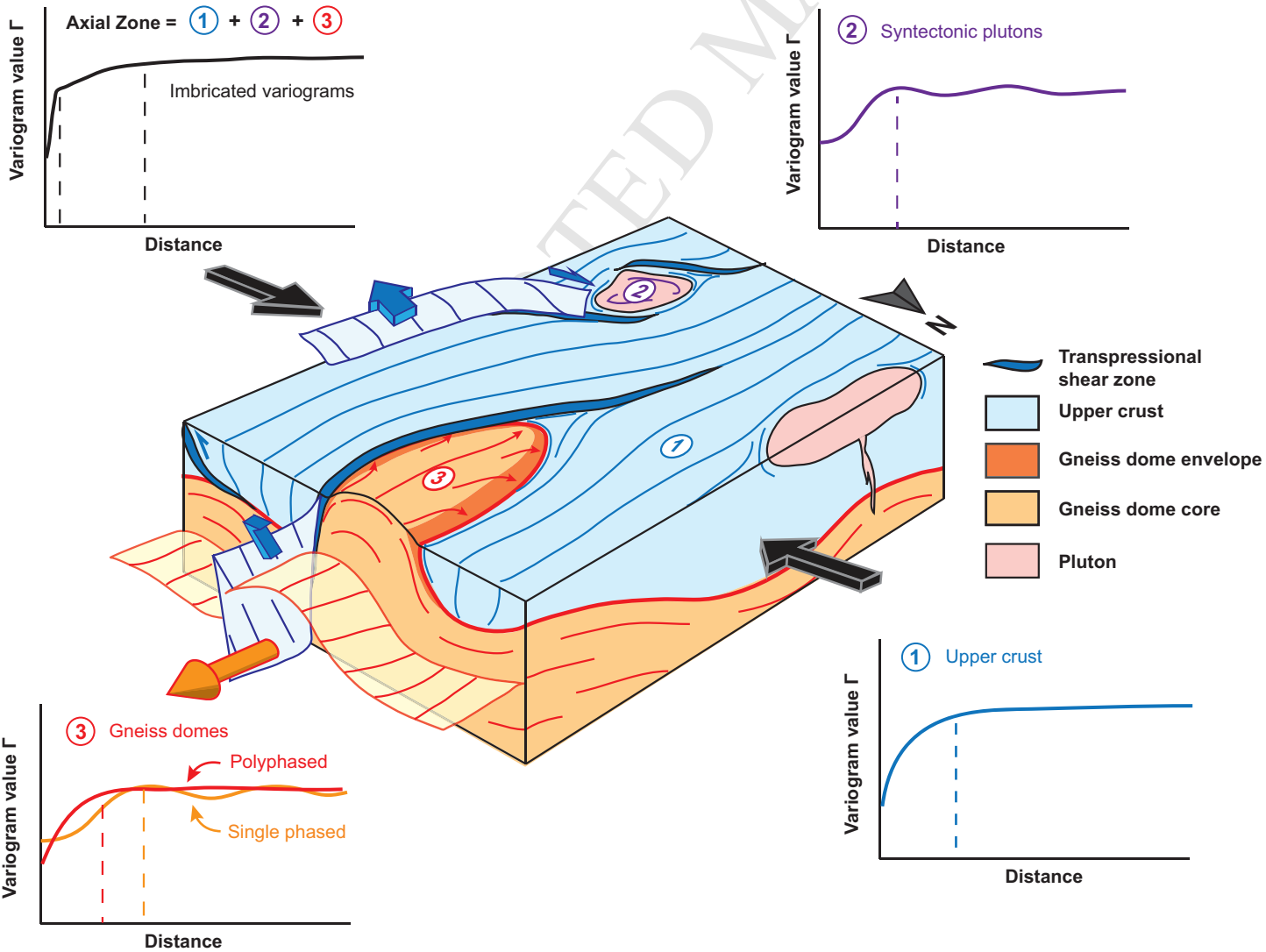

Cochelin et al. Figure 16

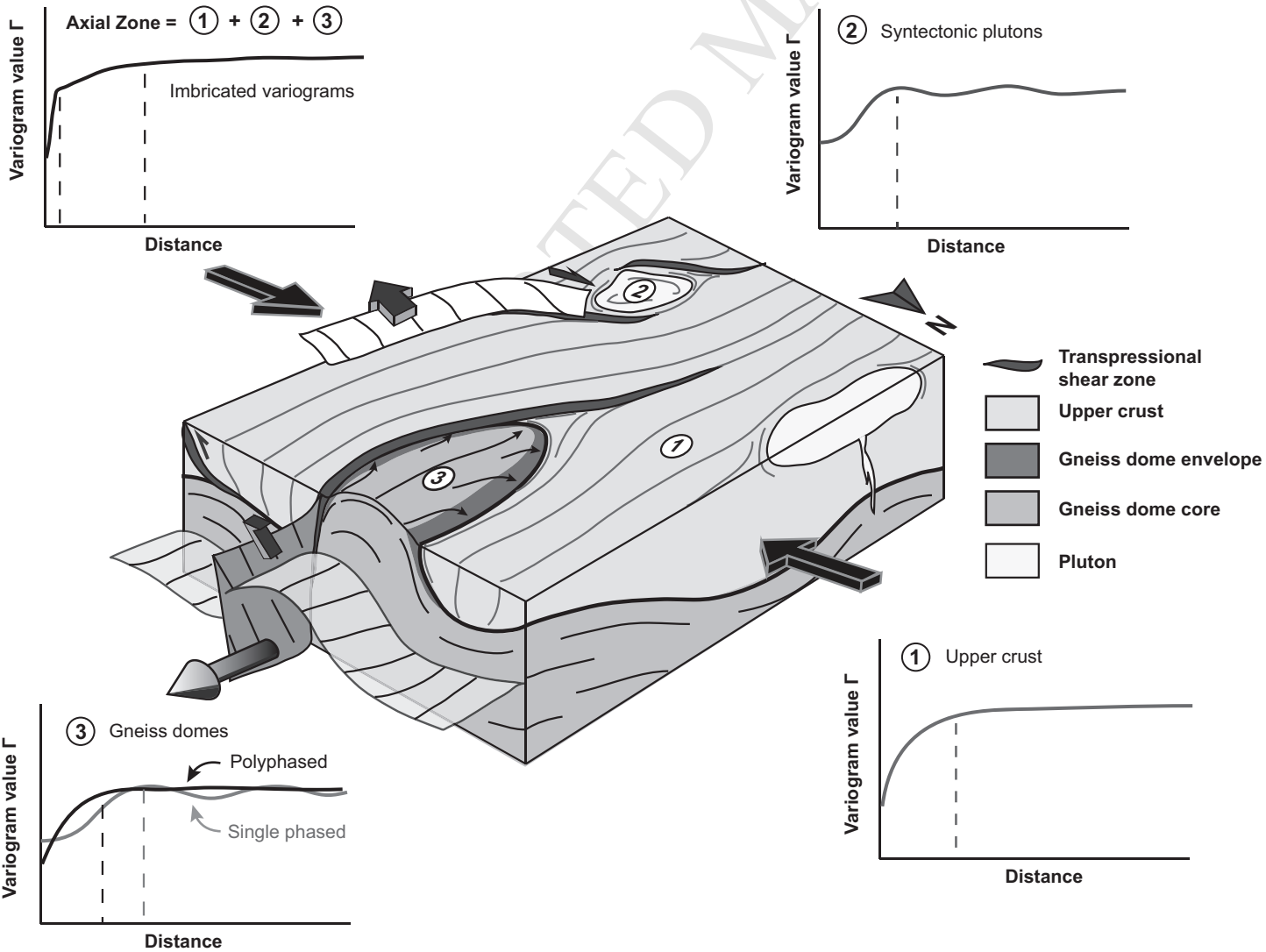

Cochelin et al. Figure 16

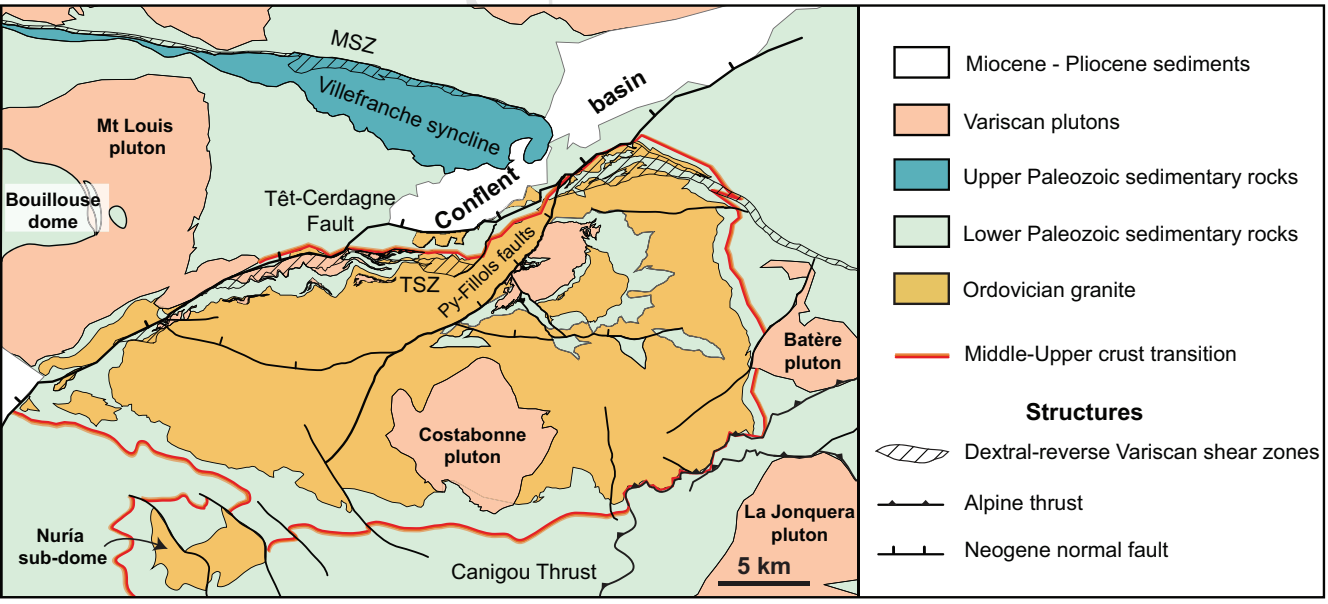

Cochelin et al. Figure 2

1 - Compilation of structural data

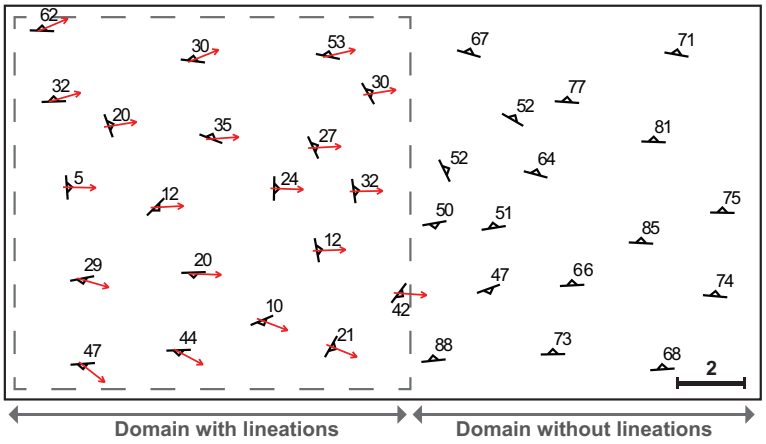

2 - Variogram calculation and analysis

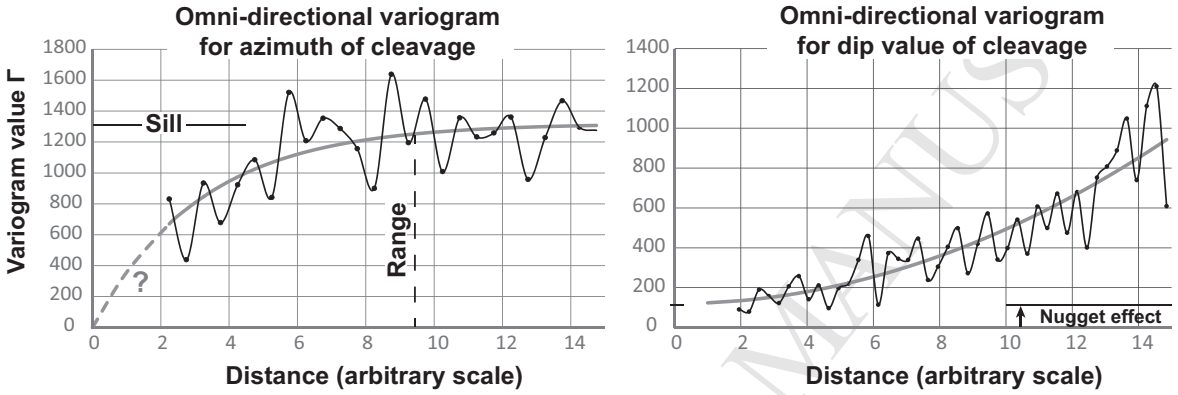

3 - Kriging interpolation

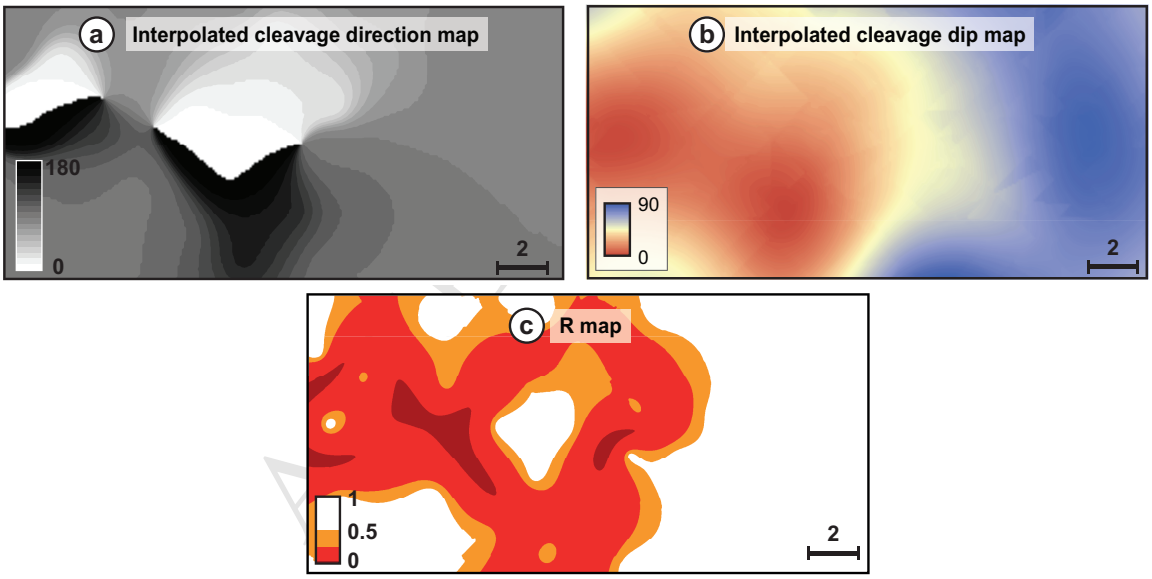

4 - Trajectories computation

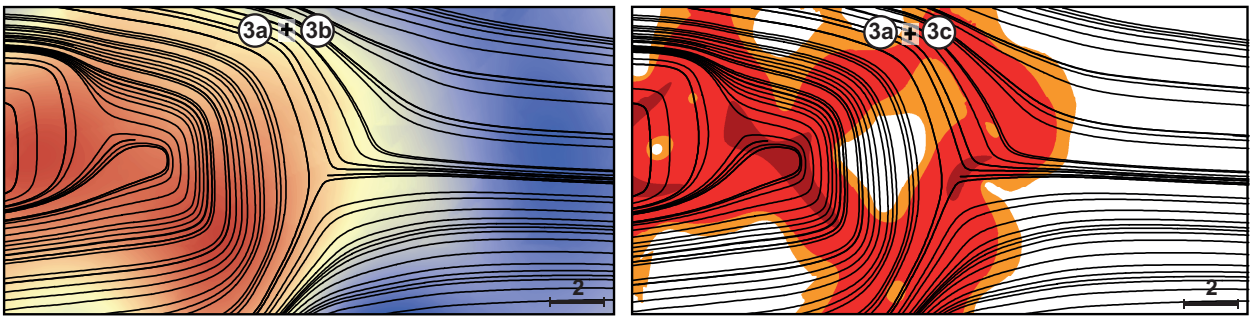

Cochelin et al., Figure 3

1 - Compilation of structural data

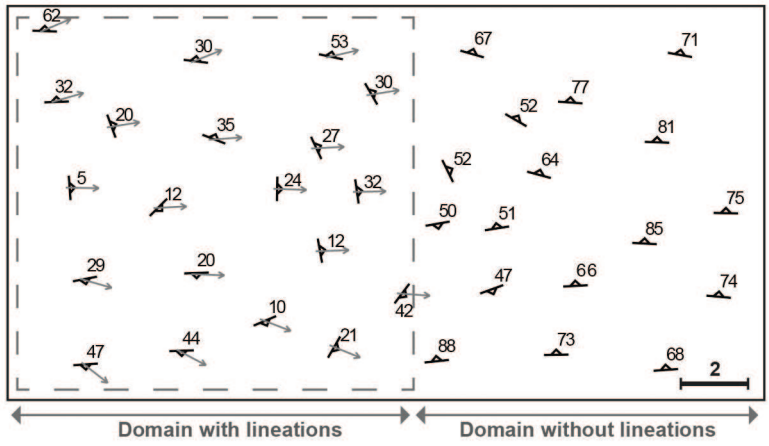

2 - Variogram calculation and analysis

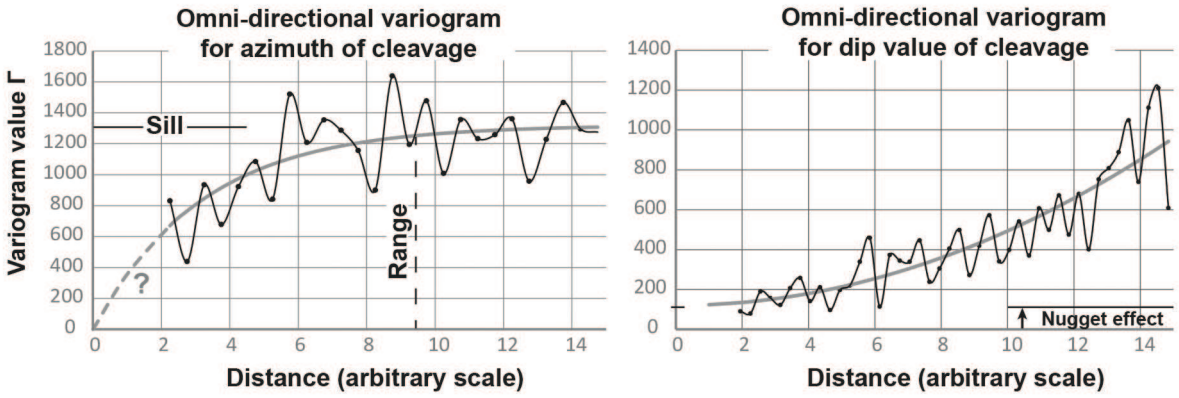

3 - Kriging interpolation

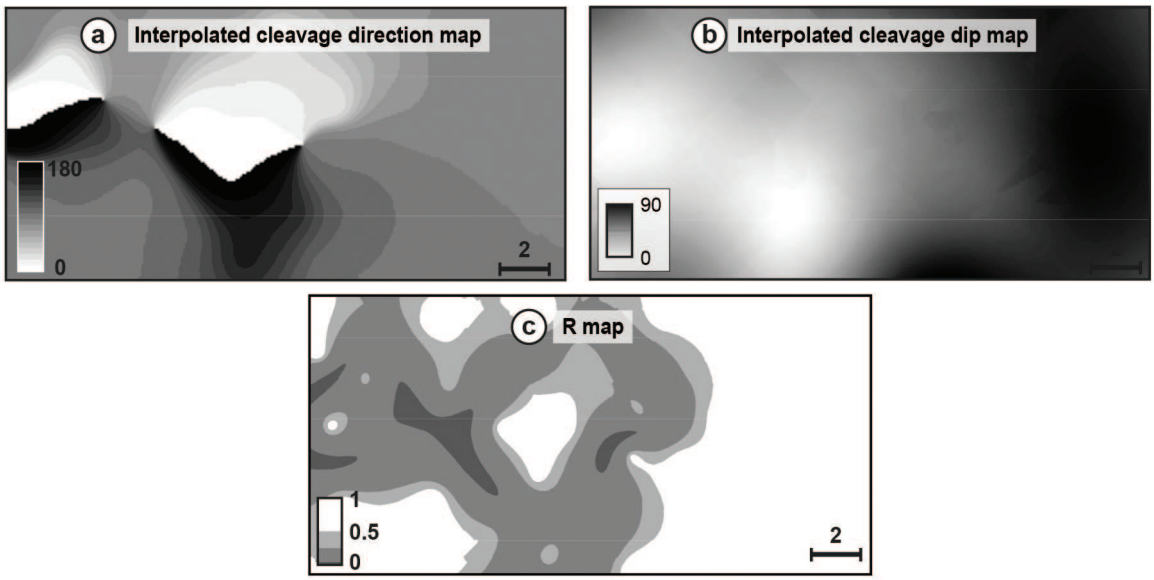

4 - Trajectories computation

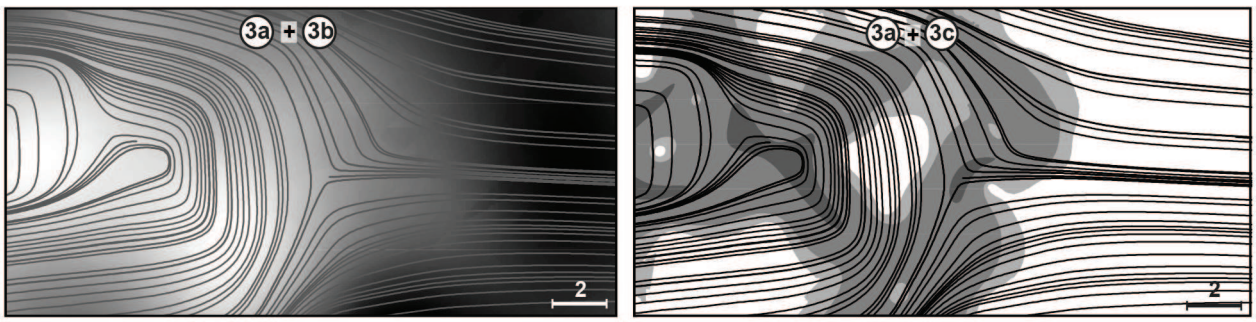

Cochelin et al., Figure 3

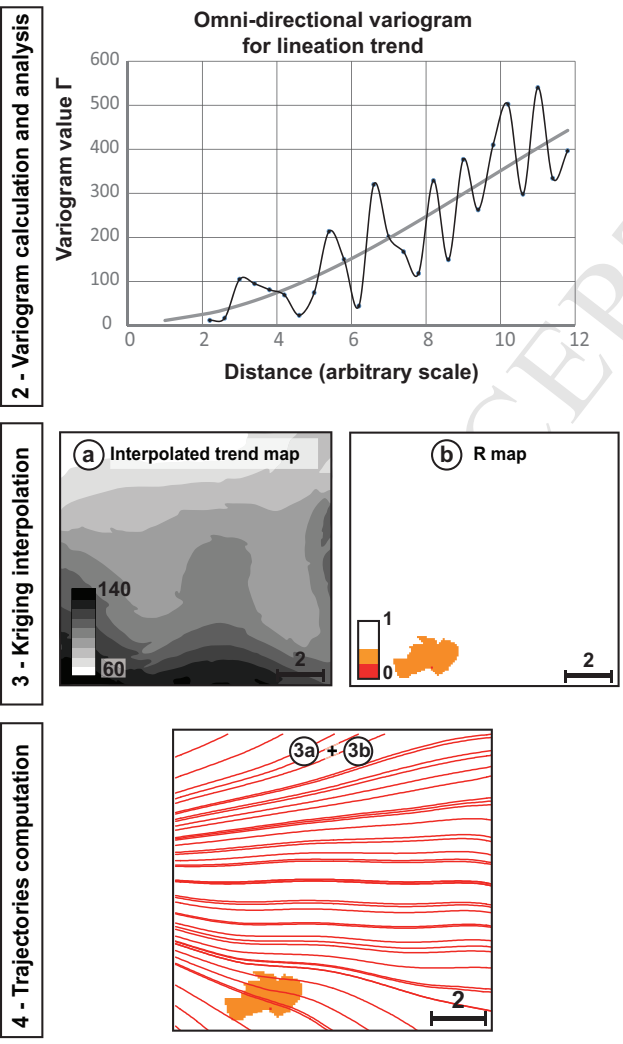

Cochelin et al., Figure 4

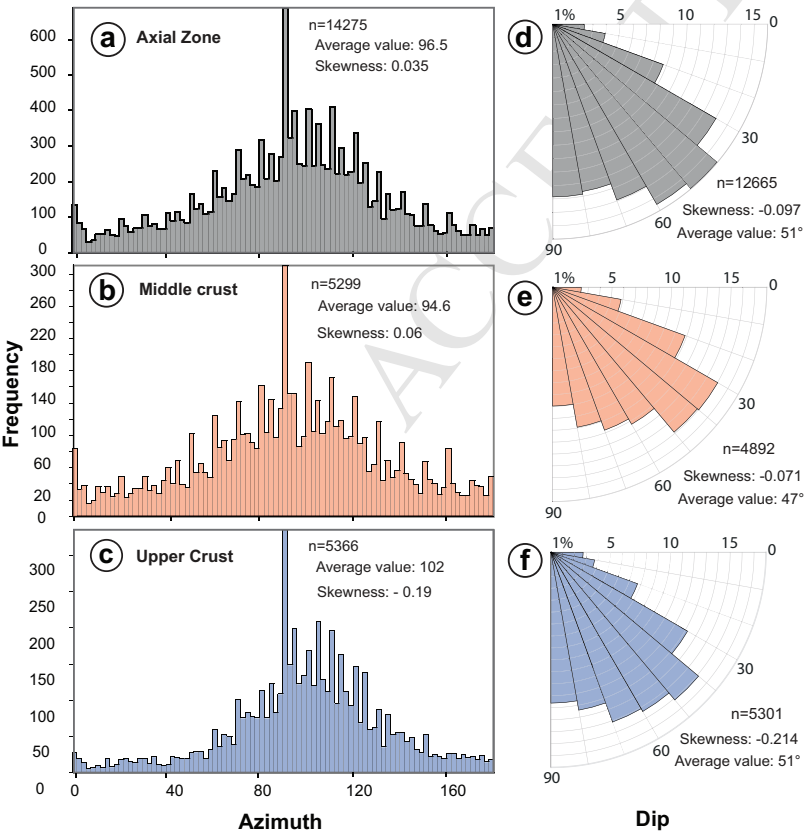

Cochelin et al., Figure 5

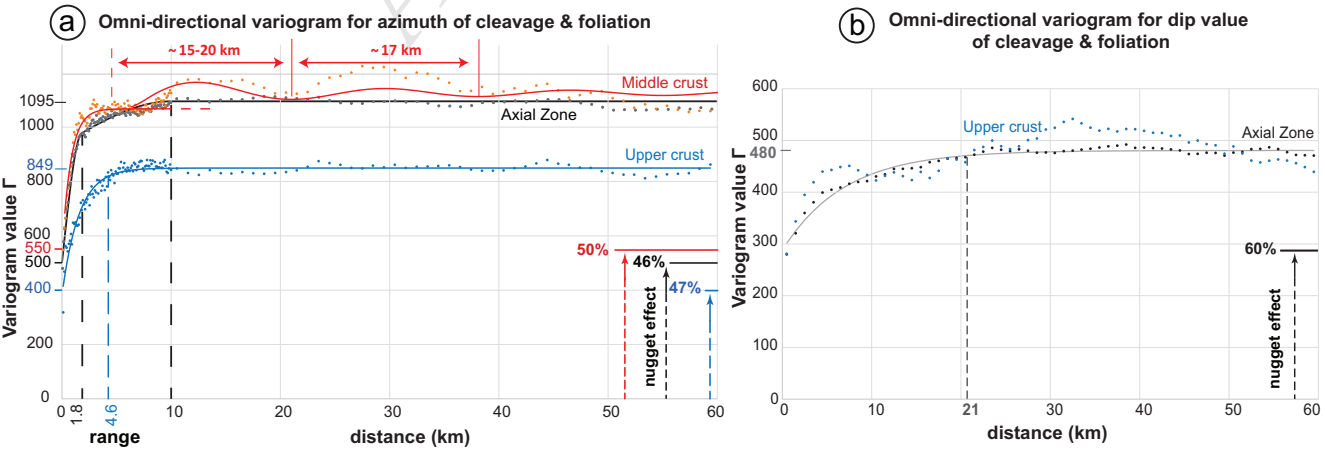

Cochelin et al. Figure 6

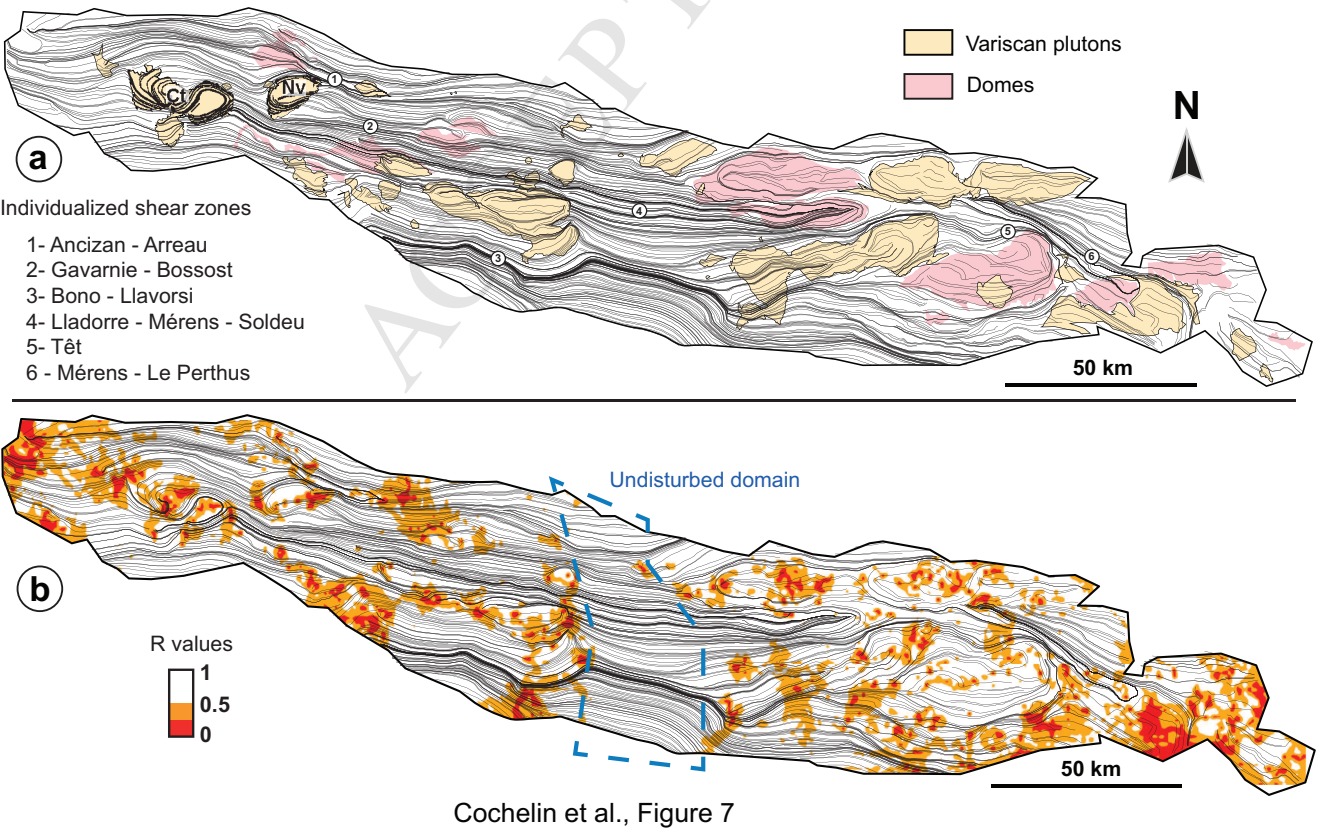

Cochelin et al., Figure 7

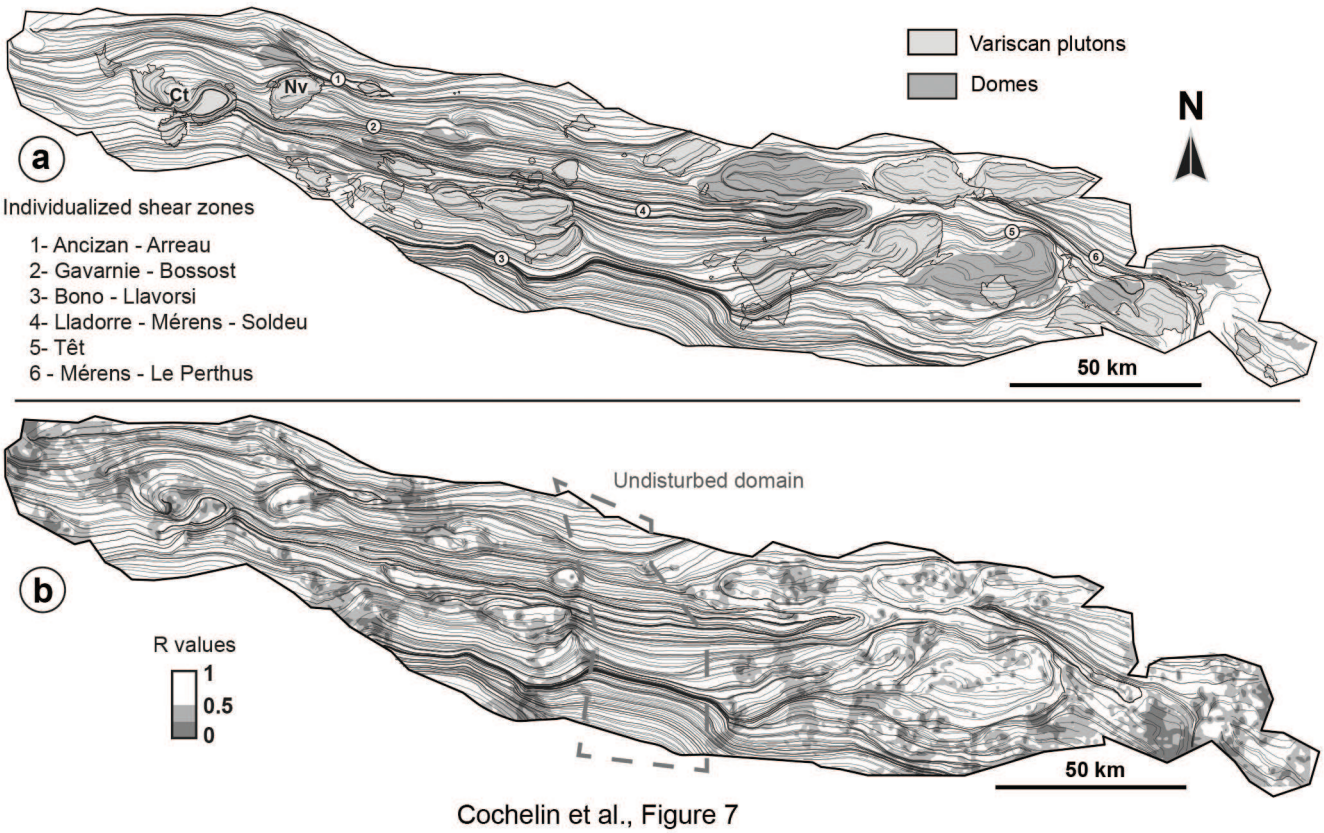

Cochelin et al., Figure 7

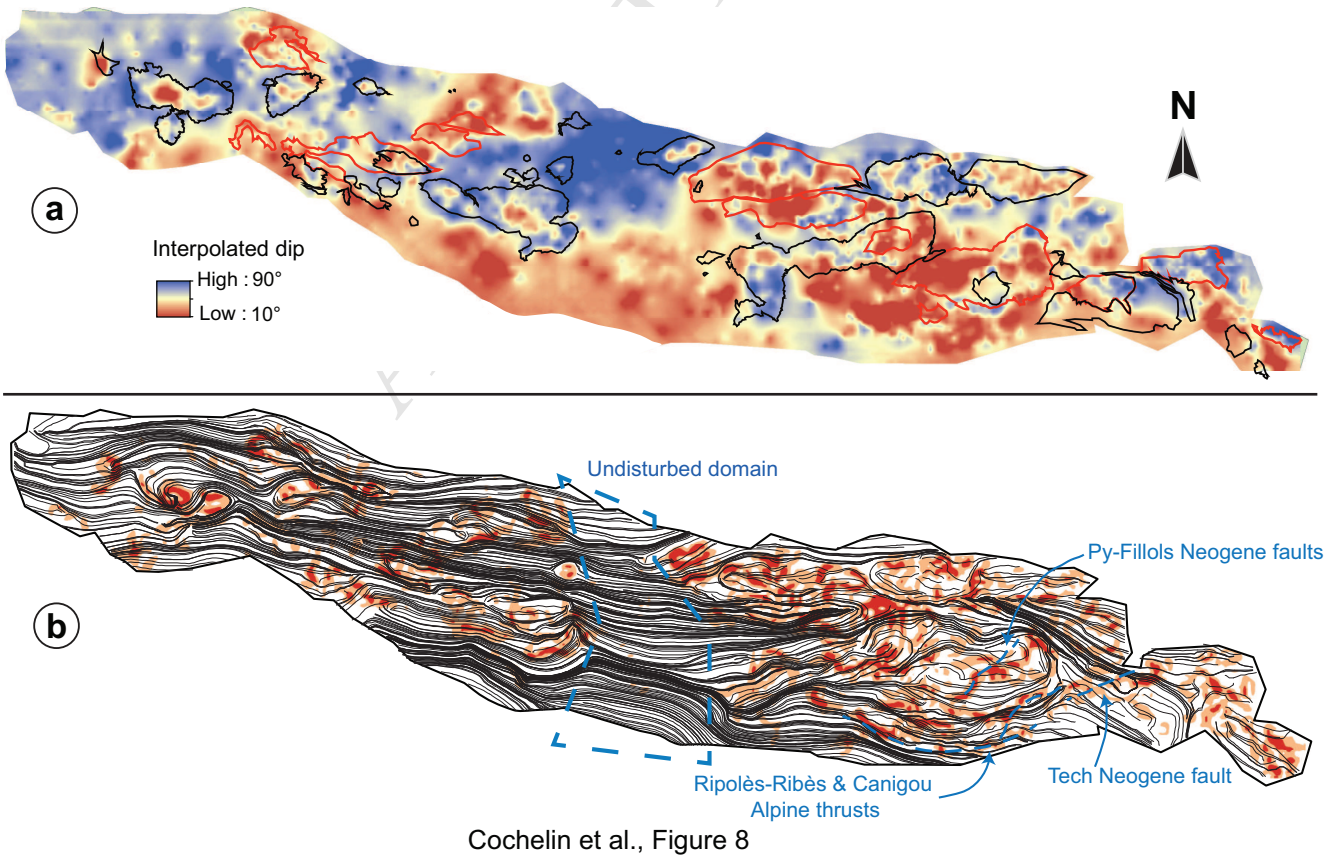

Cochelin et al., Figure 8

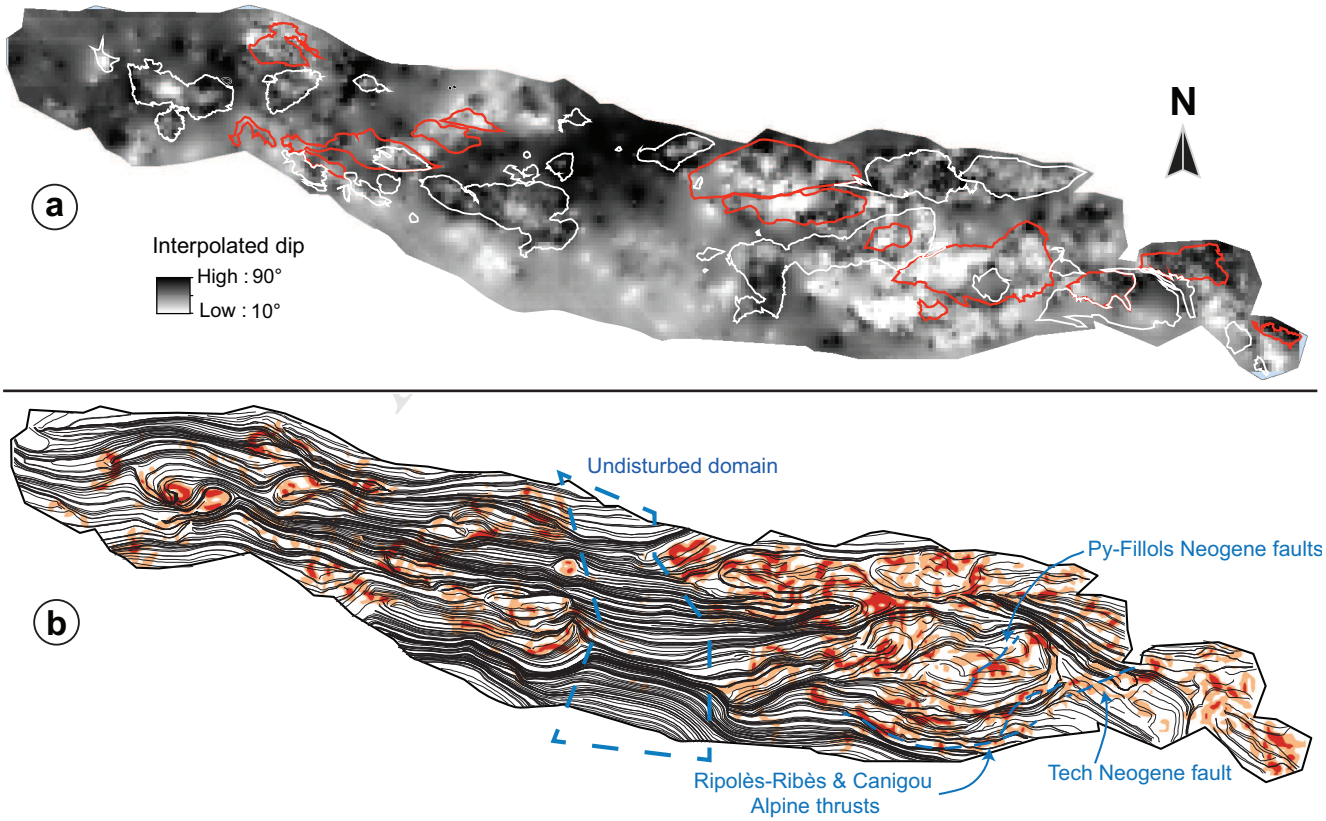

Cochelin et al., Figure 8

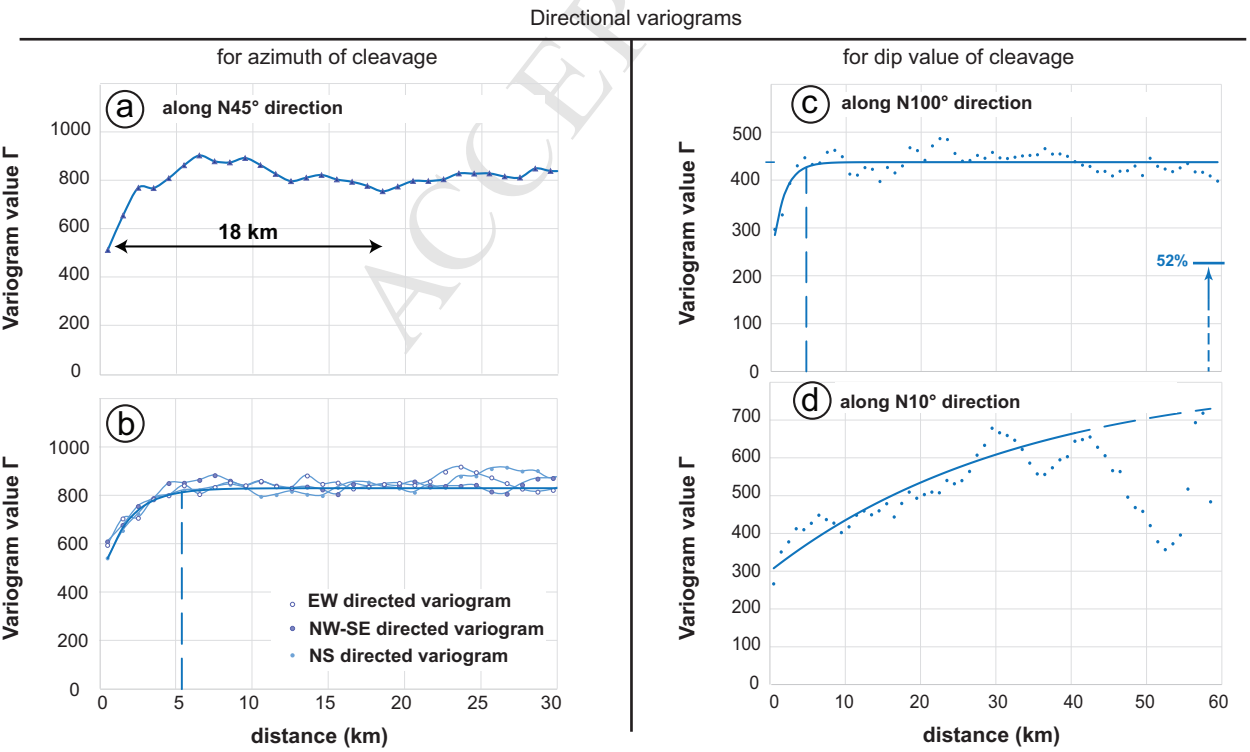

Cochelin et al., Figure 9

Highlights

- Spatial orientation variability of schistosity planes is quantified by variograms

- Building of quantitative regional and local strainfields using kriging interpolations

- The analysis of fabrics and kinematic data documents strain partitioning patterns

- Variogram analysis allows deciphering continuous from polyphased deformation